Radar tracking of synthetic particles in snow avalanches

Master's Thesis

In partial fulfillment of the requirements for the degree

"Master of Science in Engineering"

Master program:

Mechatronics & Smart Technologies

Management Center Innsbruck

Supervisor:

Dr. Anselm Köhler

Assessor:

Dr.-Ing. Sebastian Repetzki

Author:

Nico Haberstroh

221062

Declaration in Lieu of Oath

I hereby declare, under oath, that this master's thesis has been my independent work and has not been aided with any prohibited means. I declare, to the best of my knowledge and belief, that all passages taken from published and unpublished sources or docments have been reproduced whether as original, slightly changed or in thought, have been mentioned as such at the corresponding places of the thesis, by citation, where the extend of the original quotes is indicated.
The paper has not been submitted for evaluation to another examination authority or has been published in this form or another.

Place, Date Signature

Acknowledgement

I would like to express my deepest gratitude to my supervisor, Anselm Köhler. His invaluable guidance and support have been fundamental in shaping this thesis. Thanks Anselm for all your insights and direction throughout the project. The time we spent on the Nordkette, both winter and summer, was truly memorable. I am also grateful for your good explanations, proofreading and patience, especially when I struggled to keep up with your ideas. Your dedication and understanding made this journey both educational and enjoyable.

Thanks to the Austrian Research Center for Forests (BFW), Department of Natural Hazards, Unit Snow and avalanches for the provision of the resources, which were needed for this project.

Furthermore thanks to Prof. Dr.-Ing. Sebastian Repetzki for the tips and the availability.

I also want to thank the Lawinenkommission Nordkette especially Sebastian Larcher and Werner Haberfellner for making this possible, letting us on the mountain while the blasting procedure and helping to get the Radar Target inside the synthetic avalanche and always good coffee.

A huge thanks to my friends, family and flatmates for having a good time and supporting me during the thesis!

Abstract

In order to track particles within snow avalanches using a high resolution radar, an electronically amplifying radar reflector, known as Active Target (AT), is developed and characterized. The AT, in conjunction with additional in-flow sensors, allows to analyze the flow dynamics of snow avalanches at the particle level. All measurements took place at the Nordkette mountain range above Innsbruck.

The AT is analyzed and characterized including antenna aperture as well as the AT signal intensity change with radar range. Therefore calibration measurements of the static AT with different orientations at known locations were taken directly in the field of view of the mGEODAR radar. Initial tests for the moving AT scenario include roll measurements before the AT was directly placed into the avalanche. In addition to its primary function, the AT is used to calibrate the mGEODAR radar system itself by providing a known reference target to investigate ghost targets in the radar data due to internal hardware problems.

The study confirms the functionality of the newly developed AT in combination with the radar device. However, the AT antenna's polarization and aperture require alignment of the AT with the radar beam. The signal intensity of the AT is at $40\,\mathrm{dB}$ for larger ranges than $200\,\mathrm{m}$, indicating that the compensation of the geometric signal attenuation of the radar works as expected. For lower ranges, the target appears with increasing intensities that causes widening of the normally discrete target peak in the radar data. This is of minor importance for the avalanche measurements at typical distances between $300\,\mathrm{m}$ and $750\,\mathrm{m}$. Furthermore, those high intensity targets cause ghost targets at $207\,\mathrm{m}$ and $412\,\mathrm{m}$ in addition to the true target range. However, a comprehensive check of multiple radar settings does not reduce those mirror effects and the origin of ghost targets can not be identified.

One successful avalanche event has been measured with the AT and the in-flow sensor system. The rolling and flowing of the AT causes the tracked trace to appear as recurring peaks in the radar data. Nevertheless, the trace enables direct synchronization between the in-flow particle data and the radar device, and thus resolves the particle location with respect to the snow avalanche.

Contents

1. Introduction

1.1. Overview

The occurrence of snow avalanches represents a significant risk to human life, infrastructure, and natural environments in mountainous regions across the globe. A comprehensive understanding of the dynamics and flow behaviour of snow avalanches is essential for the development of effective mitigation strategies and the provision of timely warnings to vulnerable populations [1].

The conventional approach to study snow avalanches entails the utilisation of observational data obtained from remote sensing, weather stations, and visual surveys. While these methods offer valuable insights, they frequently have limitations in accurately tracking individual snow particles within avalanche flows, particularly in complex terrain or during adverse weather conditions. Recent technological advancements have seen the introduction of synthetic particles in snow avalanches, with the Austrian Research Center for Forests (BFW), Department of Natural Hazards, Unit Snow and Avalanches, playing a pioneering role in this field. These particles known as AvaNodes enable to do measurements inside an avalanche and those particles mimic the behaviour of natural snow particles, allowing researchers to study avalanche dynamics with high accuracy and reliability [2].

The application of radar technology has transformed the field of avalanche research, facilitating precise and real-time tracking of avalanche flows [3]. Radar systems are capable of penetrating snow layers and adverse weather conditions, thereby providing continuous monitoring capabilities even in low visibility scenarios. The strategic deployment of radar systems in avalanche-prone areas allows researchers to gather detailed data on avalanche dynamics, including flow velocities and runout distances [4].

A promising advancement is the combination of radar technology with synthetic particles, which are equipped with an Active Target (AT). The target reflects the signal of the radar device back and is therefore visible in the radar data. Hence, the goal is to track these particles with the radar device. For analyzing the radar data signal processing algorithms are used which enables the data to be visualized.

The analysis of radar data allows researchers to reconstruct the trajectories of avalanches, study the dynamics of flow, and operationally assesses avalanche hazard zones in a more effective manner [5]. This approach markedly advances scientific

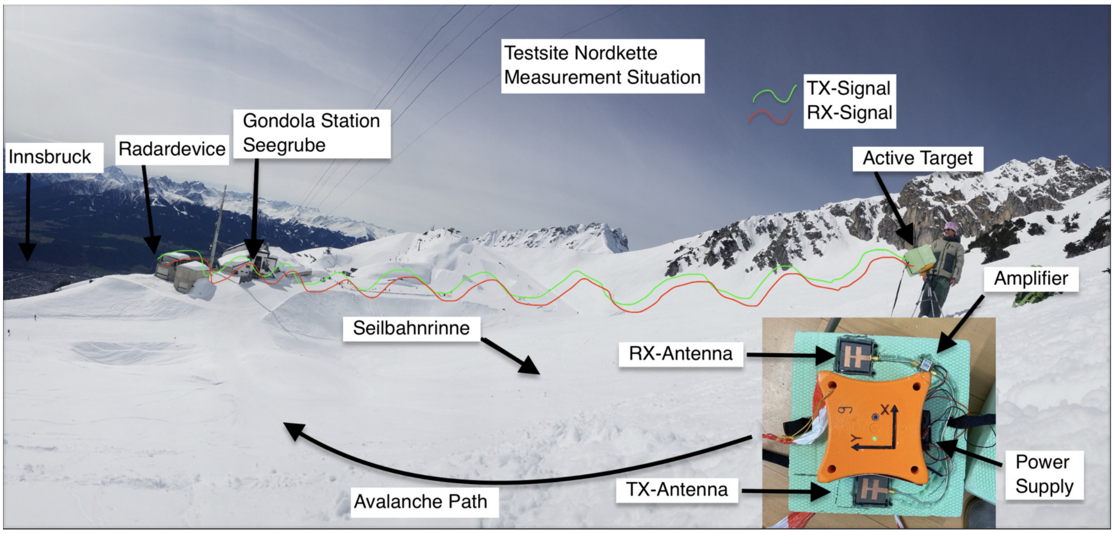

Figure 1.1.: Overview of the components in the measurement process.

comprehension of avalanche dynamics, thereby facilitating enhanced public safety and resilience in mountainous environments.

In the following this AT is developed, assembled and evaluated. The AT has the purpose to fulfill calibration measurement of the radar device and target itself and to carry out measurements inside an avalanche. The stationary radar device on the Nordkette Innsbruck will be used to track the AT and in the further process the radar settings will be analyzed in order to determine the nature of the mirror effects and ghost targets.

The photo 1.1 shows all components of a typical measurement situation. It is taken from the avalanche path in the Seilbahnrinne and comprises a side-cut of the AT (right lower corner), the radar device (middle left), transmitting and receiving signal in green and red, Innsbruck and the gondola station Seegrube. A measurement procedure involves that the radar transmits a signal (green line), the AT amplifies and returns this signal back to the radar (red line).

The lower right inset shows one of the used synthetic particles for avalanche measurement. The green foam cube includes the in-flow sensor AvaNode (orange) [2], both antennas and the battery powered amplifier. The cube is placed in the release area and as soon as a blast triggers an avalanche the radar tracks the particle along the avalanche path.

1.2. Task Definition

The principal objective is to conceive, design and evaluate an AT. It will be tracked with a radar device situated on the Nordkette in Innsbruck. The AT inside the synthetic particle, that is designed to mimic the behaviour of natural snow particles involved in avalanches. Furthermore, the AT serves as a field analysis tool, and helps to understand the radar signal to enhance the measurement accuracy.

The research entails the creation of a new cover for the AT, which is then tracked by a radar device within an avalanche scenario. In the evaluation phase, the electronic performance of the AT is tested with measurements directly in the field and in real avalanche conditions. Moreover the radar device itself is investigated with the AT that provides a known and consistent reference target.

2. State of the Art

2.1. Snow Avalanches

Snow avalanches are one of the most powerful and destructive phenomena in nature, capable of causing immense destruction to both natural landscapes and human settlements. These mass movements of snow, ice, and debris can occur in mountainous regions across the globe, posing significant risks to anyone in their path [1].

A snow avalanche typically begins with the rapid descent of a large mass of snow down a mountain slope. This is often triggered by various factors, including precipitation, wind loading, changes in temperature, instability of the snowpack, or human activity. As the snow gains momentum, it can reach speeds of more than a hundred kilometers per hour [6]. The avalanche grows during the descent by entraining snow in its flow path and can cause widespread destruction in the deposition area.

Various avalanche types have been identified, that can be summarized by their release mechanism, snow type and flow regime. For the release mechanism, one distinguishes between loose snow, glide snow and slab avalanche. Avalanche events are differentiated into dry and wet flow avalanches based on the type of snow. Especially large dry snow avalanches can evolve into powder snow avalanche that consist of a mixture of snow and air and are known for its widespread destructiveness [4].

The usual avalanche type at the Nordkette test site are released as slab avalanches of freshly deposited dry snow. The release volumes usually stay below $10\,000\,\mathrm{m}^3$ of snow, with final deposit volume up to $30\,000\,\mathrm{m}^3$.

Recently, Radar observations refined a classification based on flow regimes and seven distinct flow regimes have been identified [4]. The relevant flow regimes at the Nordkette avalanche test site are the *cold dense regime* and the *intermittent regime*. The cold dense regime avalanches usually not exceed a flow height of $4\,\mathrm{m}$. Their speed is below $30\,\mathrm{m\,s^{-1}}$ with a smooth progression of the front velocity between acceleration, a steady state and the final deceleration. Often, these avalanches occur as a single surge without internal flow features, and in terms of a radar image result in a homogeneous flowing signature. Based on these observations, it is hypothesized that these dry dense avalanches act like dry granular flows with grains in solid contact and minimal air influence, i. e. similar to flowing sand [4].

When the volume of such a cold dense flowing avalanche grows due to snow and air entrainment along the flow path, a so-called *intermittent regime* can evolve and mark

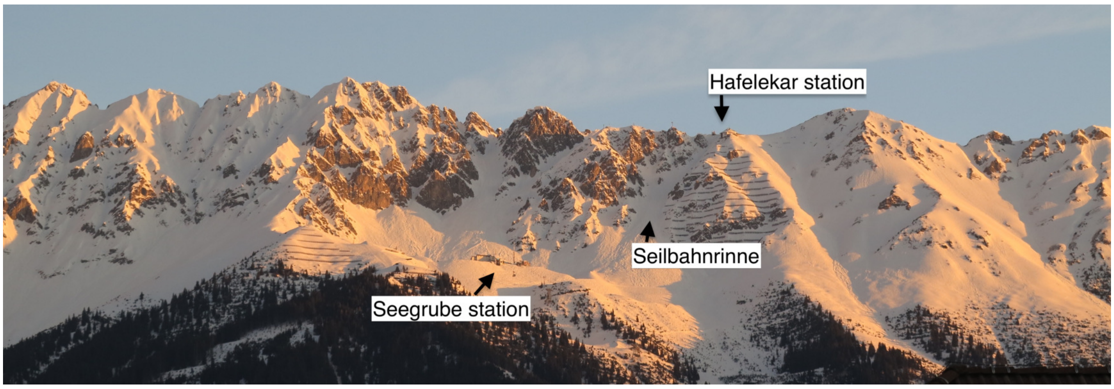

Figure 2.1.: Panoramic view of Nordkette mountain range seen from Innsbruck in the morning light. The Seegrube station is in the center, and the Hafelekar station is visible on the ridge to the right above the snow fence structures. The couloir connecting those stations is the Seilbahnrinne.

the transition towards a powder snow avalanche [7]. The air intake causes the formation of clusters of denser snow-air mixture and less dense areas inside the frontal part of the avalanche. Such a frontal region is identified by intensity streak signature in a radar image, and these streaks originate from denser clusters. Interestingly, these streaks enable to estimate the velocity of the clusters that can be up to twice as fast as the front velocity. Therefore the flowing front is constantly exchanged and overtaken by those clusters, which is known as surging and the front gets an intermittent character that is typical for powder snow avalanches.

The transition from a cold dense flow regime to the beginning of a powder snow avalanche with the characteristic intermittent flow regime is not well understood yet. Since the typical avalanches at the Nordkette are exactly at the boundary between both types, renders the Nordkette avalanche test site very valuable.

2.2. Avalanche test site

The avalanche test site Nordkette is directly reachable from the city center of Innsbruck. It is a significant mountain range and part of the larger Karwendel range (figure 2.1). The avalanche path, Seilbahnrinne, faces south and extends from the Hafelekar to the Seegrube. The total vertical drop of the avalanches is about $400\,\mathrm{m}$. The presence of a ski resort and the protection of the city is the reason for the use of explosives to trigger avalanches. This makes it an ideal location for ongoing research into avalanches and prototyping of sensors. The avalanche tests are carried out in the Karrinne, Seilbahnrinne as well as on the Osthang.

Avalanche blasting using cable cars and fuses of varying lengths is an effective method for controlled avalanche release. In this process, explosives are transported to vulnerable slopes via cable cars. These explosives are equipped with fuses of different lengths to ensure staggered detonations. This allows precise control over the explosions, enabling

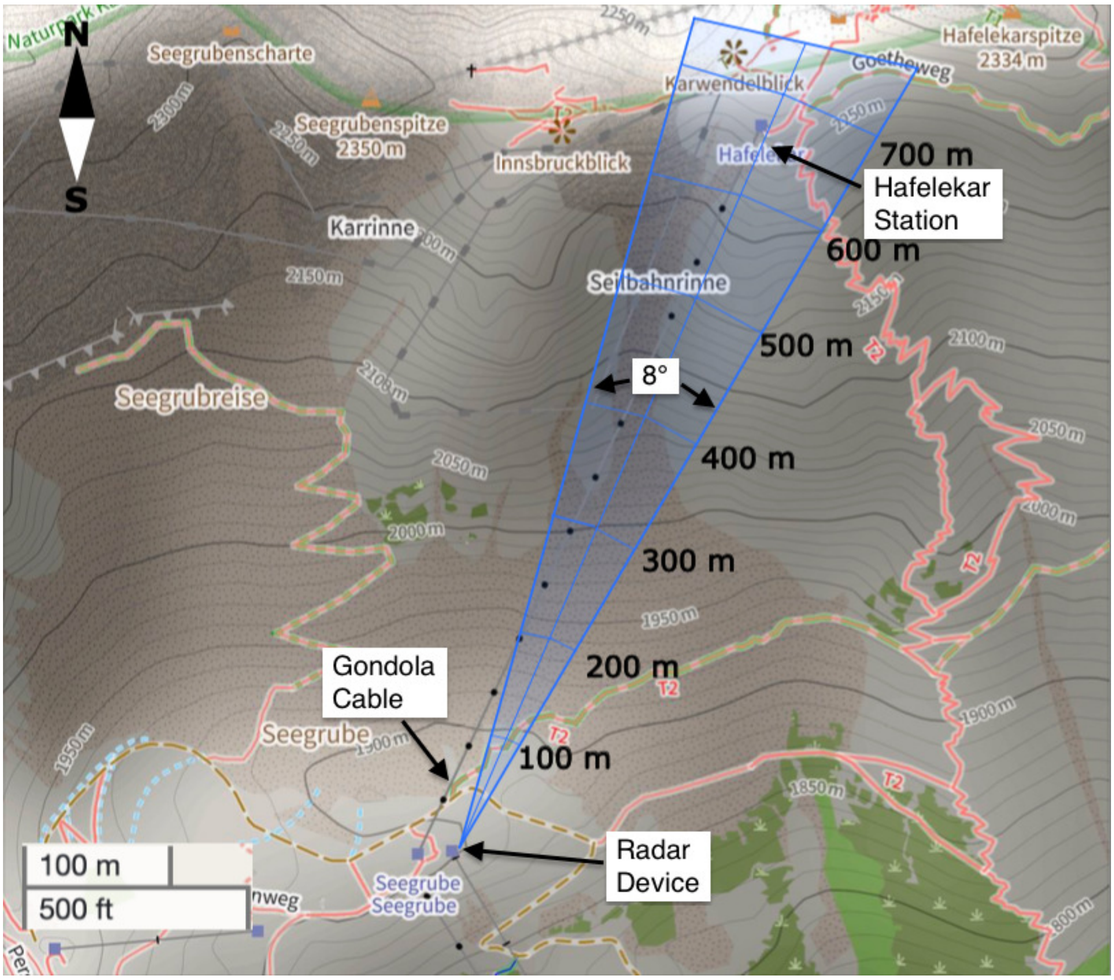

Figure 2.2.: A cartographic representation of the location of the uppointing radar device. Note: The antenna aperture (blue cone) and the indicated through-the-air radar range are only sketched and not in true scale. (Source: OpenStreetMap.org)

avalanches to be safely triggered and snow masses. This technique is frequently employed in ski resorts and alpine regions with the objective of enhancing safety and reducing the risk of uncontrolled avalanches. The blasting cableways are operated by the commission, which blasts the various sections above the ski resort and thus triggers artificial avalanches [8].

For the measurement scenarios the Seilbahnrinne plays a pivotal role in this process, as the radar device is directed at it (figure 2.2). It can be seen that the distance from the radar to the top station is about $750\,\mathrm{m}$. The radar antennas have an opening angle from left to right of $8°$ and are oriented to the Hafelekar station. In the map the gondola cable is recognizable. It starts on the left side next to the radar and ends up at the Hafelekar station. Consequently it is important to keep in mind that if the gondola is running the measurement could be affected because of unwanted disturbances of the radar signal.

Beside radar, other measurement devices are employed. A newly developed system for motion tracking within avalanches are the AvaNodes [2]. The devices are able to measure accelerations and velocities with an Inertia Measurement Unit (IMU). This

IMU can measure spatial translational accelerations, angular velocities and magnetic flux densities. Additionally there is a Global Navigation Satellite Systems (GNSS) module integrated. The utilization of this apparatus permits the measurement of latitude, longitude, altitude, Doppler velocities, world time and other data. The concave cubic shape of the AvaNodes is used to prevent rolling and sliding on the snow surface. These cubes are an integral component of the research. The avalanches are remote triggered and the cube with the measuring devices and the AvaNode will be within the avalanche. Notably, the AvaNode data are difficult to interpret without the reference from the radar data, therefore direct radar tracking of the AvaNode particles is an advantage.

2.3. Radar

The Telemobiloskop was the predecessor of the radar device, which was patented in 1904 by the German engineer Christian Hülsmeyer [9]. A RAdio Detection and RAnging (Radar) system is a device that emits a primary signal in the form of a focused electromagnetic wave. It then receives the echoes reflected by objects as a secondary signal and analyses them based on various criteria, providing information about the objects. This process typically involves determining the distance and reflecting properties such as radar-cross-section σ. The fundamental Radar equation is the radar-range-equation [10].

$$P_R = P_T \frac{G_T G_R \lambda^2 \sigma}{(4\pi)^3 R^4 L} \tag{2.1}$$

Where P_R and P_T represent the receiving and transmitting powers, respectively, G_R and G_T are the gains of the receiving and transmitting antennas, λ is the wavelength of the signal and σ represents the radar cross-section of the target. The distance is described by R and the optional factor L in the denominator of this equation can be used to represent losses, e.g. attenuation caused by the medium. In general the equation can be split in 3 different parts. The following is a breakdown of the aforementioned components. P_T, G_T and G_R are Radar constants and are summarized as C_R. The denominator $(4\pi)^3 R^4 L$ are geometries of the point target Geo_P. And σ is the effective reception area of a target.

The subsequent thesis concerns a target in an avalanche, which makes the concept of σ particularly relevant. Accordingly, the equation is formulated as:

$$P_R = \frac{C_R}{Geo_P} \cdot \sigma \tag{2.2}$$

The wavelength λ of the Radar can be written as follows.

$$\lambda = \frac{c}{f} \tag{2.3}$$

Where c is the speed of light and f the frequency spectrum. Typical frequencies are in the microwave range, which are between 0.3 to $300\,\mathrm{GHz}$, and for Radar technology usually between 1 and $120\,\mathrm{GHz}$ [10]. Wavelength λ defines the size of detectable reflectors, here in the size of snow granulate in an avalanche. The wavelength λ is $2.5\,\mathrm{cm}$ to $5\,\mathrm{cm}$ long for a Radar with 10 and $5\,\mathrm{GHz}$ respectively, therefore the powder cloud is expected to be transparent [11].

2.4. FMCW-Radar *mGEODAR*

A Frequency Modulated Continous Wave (FMCW) system principle is shown in the blockdiagram 2.3 below. It consists out of a transmitter and receiver antenna, a mixer, splitters, several amplifiers, an Analog-to-Digital Converter (ADC), a local oscillator, a 4-stage baseband filter and a system clock with a local oscillator (ADF53355). Left next to the system clock is the Direct digital synthesis (DDS) chip (AD9914) located. The power amplifier (AM31-10.2-10.7-37-37) with a gain of $37\,\mathrm{dB}$ strengthens the outgoing signal in the transmitter chain [12].

The combination of the ADC and the DDS chip allows for the effective utilisation of the full $2\,\mathrm{MHz}$ bandwidth, facilitating precise signal conversion and generation. The analog-to-digital converter (ADC) transforms the analog signal into a digital format, while the DDS chip generates an exact carrier signal that can be utilized for modulation or demodulation. Multiplexing ensures the efficient transfer of the $2\,\mathrm{MHz}$ data rate. The blockdiagram 2.3 illustrates a simplified depiction of the radar hardware. A more detailed radar structure is illustrated in section 6.3 figure 6.5.

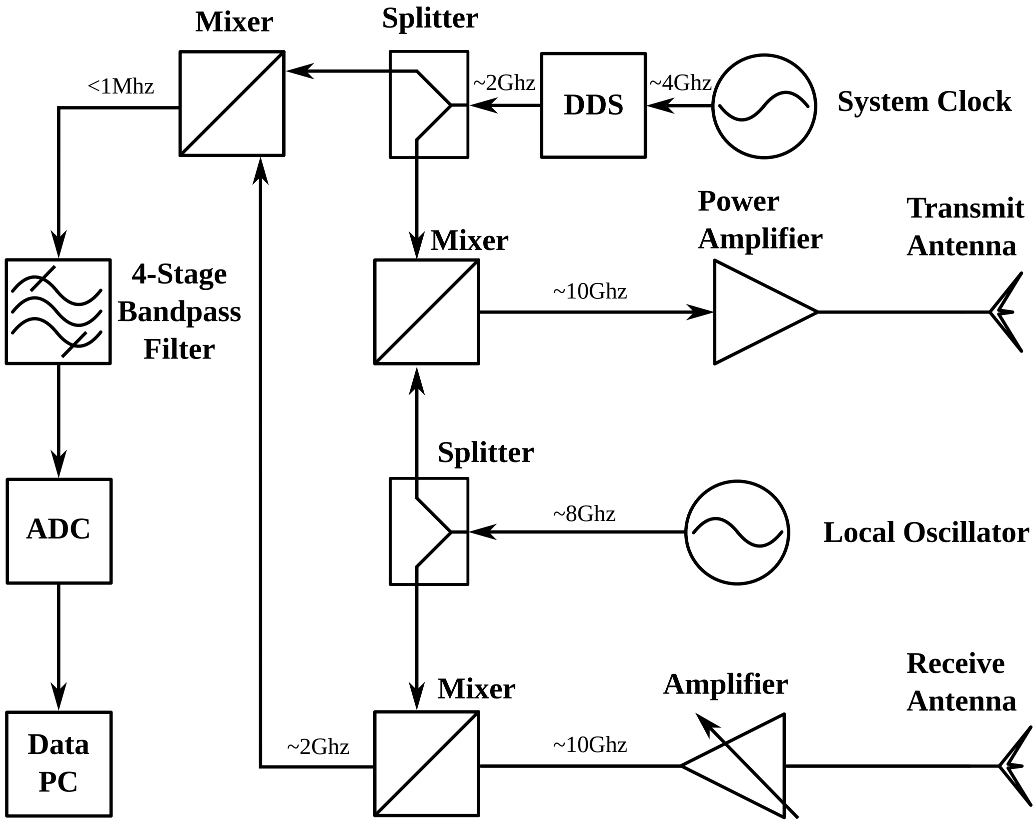

Figure 2.3.: Simple Blockdiagram of an FMCW radar system with signal processing and DDS chip [12].

The modulated signal is transmitted and received through the antennas (SA15-90-104V-D1 from Cobham) with $15\,\mathrm{dB}$ gain. The signals are recorded in the time domain with a single-channel 16-bit ADC at a maximum sample rate of $2\,\mathrm{MS/s}$ [13]. The Frequency Modulated Continous Wave (FMCW) Radar, is a type of radar sensor that transmits a continuous wave signal. Unlike a Continous Wave (CW) Radar, the FMCW Radar changes the frequency during pulses which are called chirps. The radar transmits a continuous wave at a specific frequency, which is modulated over a time period T. The Radar transmits a signal to the target, which reflects a part of it back. The reflected signal is received by the radar and compared to the original signal by mixing them and processing the resulting signal. This is illustrated in following figure 2.4.

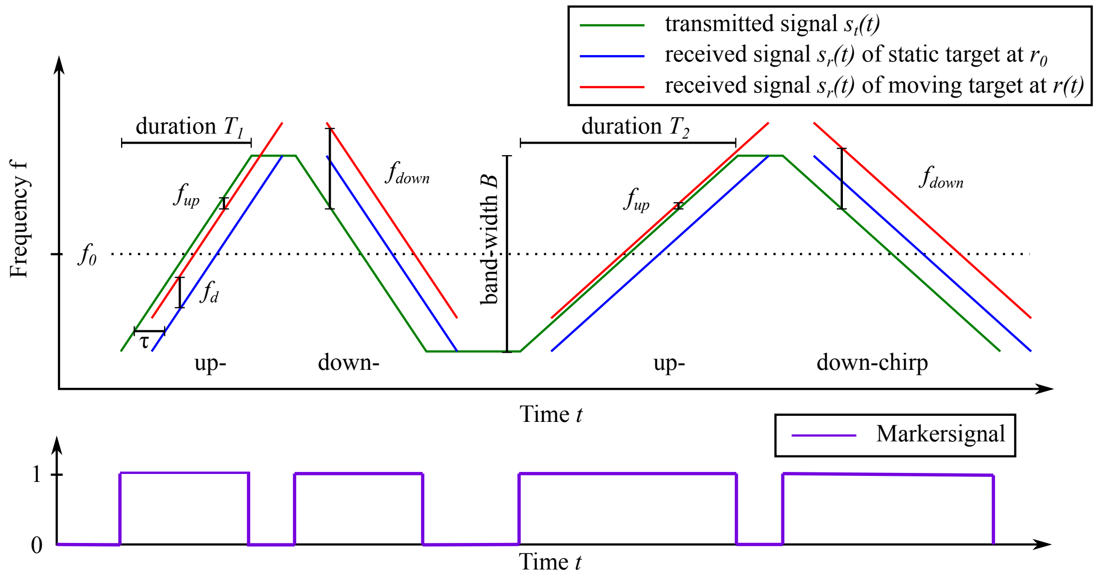

Figure 2.4.: Triangular waveform of an FMCW radar. The transmitted signal in green is received after a time-of-flight delay τ (blue), and for a moving target shifted by its Doppler frequency f_d (red). The violet line represents the digital Marker signal which indicates an active Chirp. Figure reproduced from [14].

Figure 2.4 shows the frequency f on the y-axis and the Time t on the x-axis. The green line represents the transmitted signal while the blue line shows the received signal of a static target and the red line a received signal of a moving target. The Doppler effect can be neglected because of the short time of the transmitted signals [15].

In figure 2.4 two pairs of chirps are depicted the two triangles with the flat part on the top (green line), each consisting of an up chirp and a down chirp. The characteristics of each chirp are dependent on its duration *T* and bandwidth *B* over the carrier frequency f_0. Therefore the first up chirp depends on the duration T_1. The received signal of the target whether static or moving is received with a delay of τ [13].

In order to modulate the chirp-signal figure 2.4 the DDS is needed. It divides the clock signal by 24 and generates a linear frequency ramp, the before mentioned chirp signal. With the DDS with (max. $2\,\mathrm{GHz}$) and the local oscillator (ca. $8\,\mathrm{GHz}$) the signal is mixed up to $10\,\mathrm{GHz}$. The DDS is a method of producing an analog waveform, in this case a linear frequency ramp. This is achieved by generating a time varying signal in digital form and then performing a digital to analog conversion. Due to the reason that the DDS is used digital, it offers fast switching options between the frequencies. It generates very fine frequency resolution and can operate over a bright frequency spectrum. The DDS chip is the AD9914 and provides a 400 MHz ramp. The Chip is clocked with $3.7\,\mathrm{GHz}$ [16, 12].

The signal generation hardware is the same as in *mGeodar1* since the development stage however data acquisition system was improved for winter season 2022-2023. In *mGeodar1* the used signal is recorded with two analog input channels. Due to multiplexing effects of the ADC the recording results in $0.5\,\mathrm{MHz}$. This acquisition mode is referred to *mGeodar1* [17, 12], and more complex chirp extraction is needed for data processing 4.3.

On the other hand for *mGeodar2* the ADC was reprogrammed into triggered acquisition with the marker signal (figure 2.4 violet line) from the DDS connected to a digital input and the radar signal is recorded with a single $2\,\mathrm{MHz}$ channel. The digital marker signal is essentially a signal from 0 to 1, which provides the trigger for the chirp to commence and cease its operation. This can be seen in figure 2.4 indicated with the violet line. In the case the marker signal equals one, the chirp pulse undergoes an upward or downward direction. Conversely, when the signal is equal to zero, the actual position remains unchanged. With the ability of recording in $2\,\mathrm{MHz}$ the data results in a much better resolution. The received signals are analysed by a signal processing unit.

There are several modulations for the chirps that are used in a FMCW radar such as triangle, Sawtooth and sinusoidal. In the illustration 2.4 a triangular model with pauses after up and down chirp is considered. The received signal for the static target is represented by the red line and is subject to a time delay of τ. The blue line represents the moving target and also includes the Doppler frequency f_d in the received signal [14].

The signal reflected from the target experiences a time delay of τ. This delay can be used to calculate the target's range using the following formula 2.4, where R_0 describes the line of sight range from radar to target, which is twice the distance travelled by the signal to reach the target and return to the radar system, the speed of light is denoted by c, v is the velocity of the target in $\frac{m}{s}$ and T is chirp duration in seconds [18].

$$\tau = \frac{2(R_0 - vT)}{c} \tag{2.4}$$

Either for a static target with a speed of $v = 0\frac{m}{s}$, or a sufficient short chirp duration T the distance R_0 is directly related to the time delay τ which is the time of flight of the radar signal.

$$R_0 = \frac{c}{2}\tau \tag{2.5}$$

Pulse radars directly measure the τ whereas Frequency Modulated Continous Wave (FMCW) radars substitute the timing measurement with frequency measurement that can be achieved more effectively with high resolution.

Therefore the basic principle for an FMCW Radar is to transmit a waveform of constant amplitude A_0 with a linear Sawtooth variation of frequency figure 2.4. This is the reason to use an FMCW radar because the ranging with frequency measurement is much easier than the time-of-flight measurements. The frequency difference from the echo signal to the transmitted signal is directly proportional to the target. Therefore it is more accurate and easier than measuring extremely short time intervals, especially given the speed of light 2.11. Small errors in the time measuring can lead to significant errors in distance calculations. Therefore measuring the frequency difference is easier.

The use of a FMCW radar is justified by the fact that ranging with frequency measurement is a more straightforward process than time-of-flight measurements. The frequency difference between the echo signal and the transmitted signal is directly proportional to the target. Consequently, it is more accurate and easier than measuring extremely short time intervals, particularly given the speed of light 2.11. Errors in time measurement can result in significant errors in distance calculations. Consequently, measuring the frequency difference is a more straightforward process.

A linear chirp signal a(t) is transmitted equation 2.6.

$$a(t) = A_0 \sin 2\pi(f_0 t + \frac{1}{2}\alpha t^2) \tag{2.6}$$

Where α is the chirp rate (see 2.4.1). The received signal b(t) consists of the above equation and a time delay tau τ.

$$b(t) = b_0 \sin 2\pi[f_0(t-\tau) + \frac{1}{2}\alpha(t-\tau)^2] \tag{2.7}$$

Both amplitudes of the two signals are related to each other with the fundamental radar equation 2.1. In the receiver chain the signal is mixed with the transmitted signal.

$$s(t) = a(t) \cdot b(t) \tag{2.8}$$

The resulting signal $s(t)$ contains the sum and the difference frequency of $a(t)$ and $b(t)$, thus a high frequency and a low frequency part. An analog low pass filter let pass the low frequencies which is usually called beat frequency f. The filtered signal $s(t)$ is proportional to

$$s(t) \propto \cos(\frac{2}{c} \cdot \alpha \cdot r \cdot t) = \cos(f \cdot t)\,. \tag{2.9}$$

It is this low frequency signal which is digitized with the ADC. The low frequency signal is related to the desired range of the target r, and no time measurement needed any more as indicated by equation 2.5.

2.4.1. FMCW variables

The description of a linear pulse in an FMCW radar involves the bandwidth *B* and the pulse duration T, which can be illustrated with the chirp rate $\alpha = \frac{B}{T}$. From equation 2.9, the target distance *r* follows from a relation between this chirp rate α, the measured beat frequency *f* together with the signal propagation velocity *c*.

$$r = \frac{c \cdot T}{2B} \cdot f = \frac{c}{2\alpha} \cdot f \tag{2.10}$$

Using c being approximated by the speed of light c_0 in vacuum, with μ_0 the vacuum permeability $\mu = \mu_0 = 4\pi \cdot 10^{-7} \frac{Vs}{Am}$ and the vacuum permittivity $\epsilon = \epsilon_0 \approx 8.854 \cdot 10^{-12} \frac{As}{Vm}$ [19].

$$c_0 = \frac{1}{\sqrt{(\mu_0 \epsilon_0)}} = 299792458 \frac{m}{s} \tag{2.11}$$

Note, the Doppler effect which is relevant for moving targets, also causes a frequency shift in equation 2.10 by the Doppler frequency $f_d = \frac{2 \cdot f \cdot v}{c}$. The range uncertainty by this Doppler shift is usually less than $2\,\mathrm{m}$ for the typical velocities and frequencies, and usually neglected. However, this shift can be utilized to determine the speed of a target with more advanced waveforms and processing techniques [14].

It can be shown, that the range resolution Δr for a FMCW radar, and therefore the ability to distinguish two separate targets from each other, only depends on the bandwidth of the chirp and can be calculated in equation 2.12 [10].

$$\Delta r = \frac{c}{2 \cdot B} \tag{2.12}$$

The maximum range capability of a FMCW radar system is determined not only by the parameters outlined in the radar equation 2.10 but also by the speed of the ADC in the receiver acquisition hardware [20], e.g. the Nyquist frequency defines maximum frequency and therefor range in equation 2.10.

2.4.2. Basebandfilter

Prior to the ADC, a four stage baseband filter is situated which fulfills the following three functions aliasing, cross-coupling and geometric attenuation.

All frequencies that are too high and would result in aliasing effects are damped. The direct cross-coupling between the antennas of the radar device, for example very little range *R* results in low frequency equation 2.10, is prevented through the damping of the lower frequencies. Additionally, the objective is to provide distance-specific leveling of the signal strength, as the signal attenuates with $1/r^3$ due to geometric reasons equation 2.1. This is accomplished by amplifying the larger beat frequencies, which correspond to greater distances, while the smaller ones are less amplified or even attenuated. It consists out of four filter stages. Each stage is an active bandpass filter and can be adjusted using digitally controlled switches [12].

2.4.3. FMCW-Radar mGEODAR on the Nordkette

The used FMCW radar on the Nordkette mGEODAR was first installed by Anselm Köhler and has the following configuration.

Table 2.1.: FMCW radar configuration

Bandwidth (B)	$400\,\mathrm{MHz}$
Center carrier frequency (f_0)	$10.4\,\mathrm{GHz}$
Frequency band	$10.2\,\mathrm{GHz}$ to $10.6\,\mathrm{GHz}$
Chirp duration (T)	$10\,\mathrm{ms}$
Wavelength (λ)	$0.025\,\mathrm{m}$

With the given Bandwidth B and the before mentioned equation 2.12 it is possible to calculate the range resolution Δr_N for this FMCW-radar.

$$\Delta r_N = \frac{299792458\frac{m}{s}}{2 \cdot 400 \cdot 10^6 Hz} = 0.3747405725m \tag{2.13}$$

In the following photos 2.5 the installed device on the Nordkette can be seen.

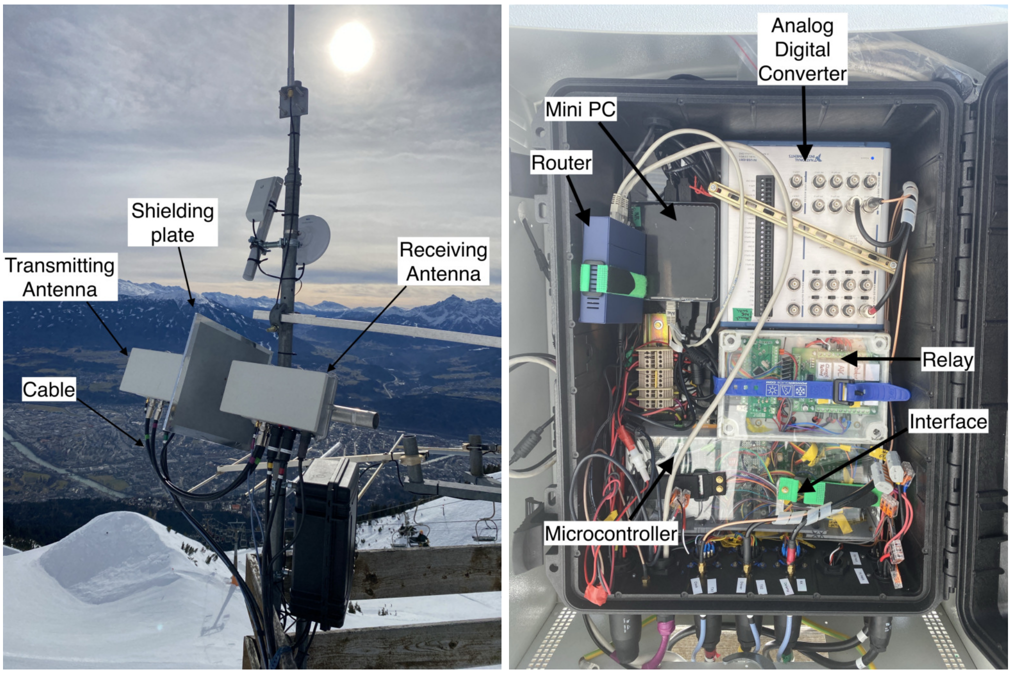

(a) Radar device (b) Radarbox

Figure 2.5.: Radar device and associated hardwarebox.

Photograph 2.5a includes the Radar device with the two receiving and transmitting antenna and the shielding plate to prevent cross-coupling in between. The FMCW hardware from the blockdiagram 2.3 with DDS, Local oscillator, Splitter, Amplifier is located in front of the transmitter Antenna and the Pre-Amplifier, Mixer, Basebandfilter 2.4.2 in front of the receiver Antenna. A shielding plate is situated between the two antennas, thereby preventing the two antennas from coupling with each other. The right-hand side of Figure 2.5b. This component constitutes the core of the radar device. The device comprises an ADC, a mini personal computer (PC), a router, a microcontroller, a relay, and an interface. The mini PC enables the device to be controlled and also to save the received data. The router provides the device with internet connectivity. The ADC transforms the analogue signal emitted by the radar into a digital signal, which can then be utilised by the PC. The transfer of data from the radar to the laptop is conducted via a cable, an external hard disc that is connected to the mini PC or via WLAN (wlan) [17].

Since the initial installation in winter season 2020/2021, more than 200 avalanches have been successfully recorded. However, some of these measurements contain errors which look like additional avalanches, but are in fact multiple occurrences of the same avalanche at shifted ranges. The origin of these duplicated images, or herein generally called ghost targets, is still completely unclear but most likely are caused by internal reflections or mirror effects in the radar hardware. Therefore the radar signal needs thorough investigations.

2.5. Active Target (AT)

An Active Target (AT) is a type of radar reflector that actively amplifies the incoming signal and transmits this signal back into the incoming direction. A simple schema for an AT is sketched in the block diagram 2.6, where the two antennas are indicated with Receiver Antenna (RX) and Transmitter Antenna (TX) based on the directionality of the amplifier.

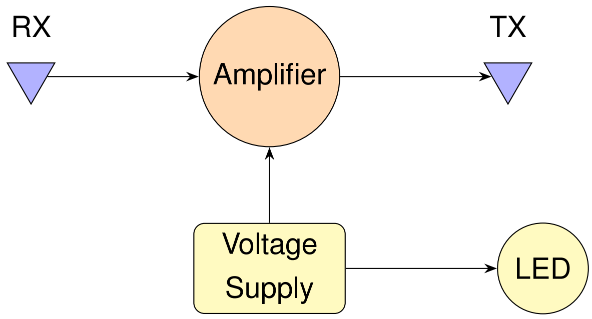

Figure 2.6.: Simple block diagram of the AT

Such an AT proved useful in the development of the predecessor radar GEODAR in the Swiss test-site Vallee de la Sionne [14]. Their AT is permanently installed in the middle of the avalanche track and represents a defined target throughout the whole winter seasons and is primarily used to ensure the radar operates properly. A second AT is in a mobile configuration and used for calibration purposes.

The components for an AT for the frequency range of the mGEODAR exist, but were only shortly used for quick tests during the radar development and initial avalanche measurements [21]. The results of these measurements were solely to prove the correct orientation of the radar antennas, but a complete characterization of the AT has never been done.

3. Goal

The goal is to combine the methods of tracking synthetic particles inside avalanches with the help of radar observation. Another objective of this thesis is to investigate the capabilities of the radar system "mGEODAR", installed on the Nordkette Innsbruck, with the developed AT.

In a first step, an AT is developed and its performance is tested and characterized in the field using the mGEODAR radar as a signal source.

In a next step, the AT facilitates for calibration and validation of the radar system, and to minimize and optimize artifacts or inaccuracies inherent in the radar recordings. The focus is on two problems of the radar hardware. Firstly, the radar suffers from spectral leakage, so that targets may appear larger than they are. Secondly, mirror effects or internal reflections exist in the radar hardware causing ghost targets to appear in the data in regular range intervals.

Lastly, the aforementioned synthetic measurement particles AvaNodes are equipped with the AT. This particle is then embedded onto the snowpack prior to an artificial avalanche release. The avalanche together with the particle is successfully tracked by the mGEODAR radar device. The particles mimic the flow behavior of snow particles enabling to study avalanche dynamics.

4. Methods

4.1. Concept of Active Target (AT)

The target comprises the components enumerated in section 2.5. The two antennas, one for RX and one for TX, serve as the heart of the target. The RX receives the radar waves, and the signal passes through the amplifier, becoming stronger before reaching the TX to be returned. The signal then returns to the radar device, completing one cycle. Thus the target is identified with a strong peak in the radar data at the range from target to radar.

The first step is to figure out if the antennas are polarized and if so, in which direction it needs to be kept for successful measurements. Therefore different alignments of the antennas are investigated. The validation of the data results in following orientation of the antennas figure 4.1a. Once the orientation is determined, the various points shown in the illustration on the right 4.1b were run through. Chapter 6 presents the results of these measurements.

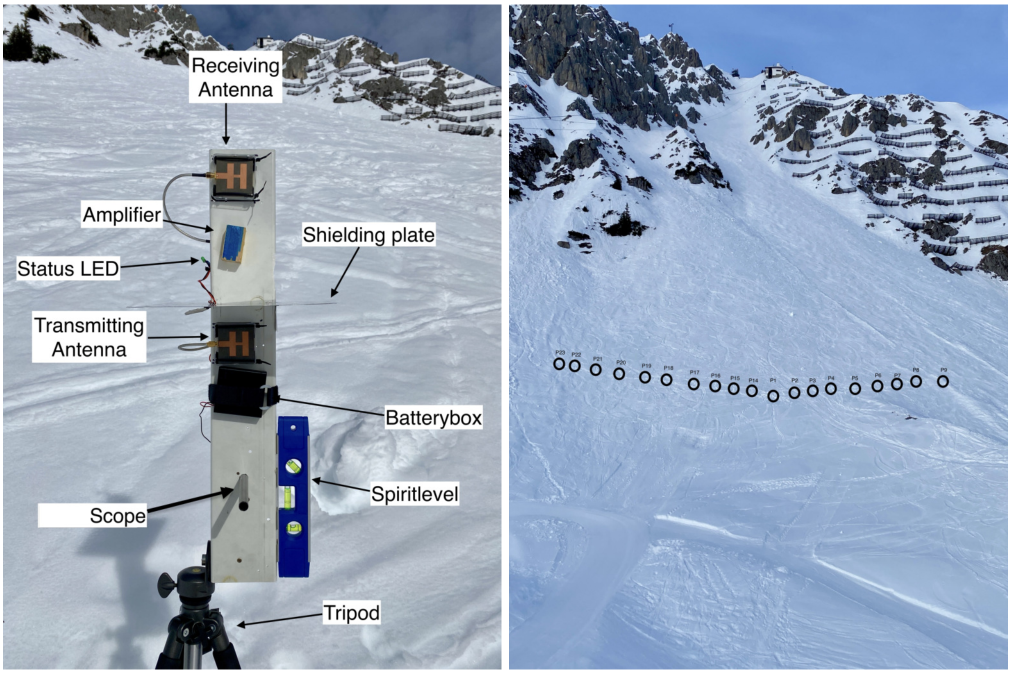

(a) Experimental Setup (b) Measurement Points

Figure 4.1.: Measurement situation Nordkette in the Seilbahnrinne with the first Prototype of the AT on the left side and the different measurement points on the right side.

The photos 4.1 were taken on the Nordkette Seegrube, where the radar device is pointing towards the Seilbahnrinne which can be seen in the picture on the right side 4.1b. The setup 4.1a of the AT includes a spirit level, a scope, a battery box, an amplifier, and two $10\,\mathrm{GHz}$ antennas where one is receiving and the other one transmitting. Additionally a GPS module was there for determining the exact position. Therefore the distance between radar and the measuring position can be detected. The spirit level and the scope aid in aligning the AT with precision. In order to ascertain the likelihood of the target being observed, the scope is employed to point directly on the Radar. That's caused by a good alignment of the antennas. The battery-box is needed for the voltage supply of the amplifier. The requisite voltage of the amplifier is $5\,\mathrm{V}$. For this reason a power supply with output voltage of $5\,\mathrm{V}$ is used. The way the AT works is that the transmitted waves from the Radar are picked up by the receiving antenna from the AT, passed through the amplifier, amplified by a factor and sent back to the receiving antenna of the radar unit with the transmitter antenna of the Target. The status LED is employed for the purpose of verifying the sufficiency of the voltage supply. The shielding plate serves to ensure that the antennas are not subject to cross-coupling like the radar device figure 2.5a.

The right photo 4.1b shows a first measurement scenario in the Seilbahnrinne. On top of the picture there is the top station of the Nordkette. The experimental site, designated as the Seilbahnrinne is situated within the downward-facing channel. The black circles in the middle of the picture constitute the measurement points starting from 1 to 23. Point 1 is in the middle of the photo. Outgoing from this point the measurement started to the right side till point 9. Again outgoing from point 1 the left side was done in the same matter from point 14 to 23. The aforementioned procedure was designed to facilitate the calibration method described in section 4.5.

4.2. Data collection

The measurements vary between calibration measurements, roll measurements and avalanche measurements. The calibration measurements are employed for the purposes of both calibrating the target and calibrating the radar. For this reason measurements with and without the AT were conducted. Prior to undertaking any measurements, it is necessary to ascertain that the radar is operational. Consequently, it is possible to operate the radar remotely. The duration of calibration measurements is for one second. In contrast, the roll and avalanche measurements are ranged from several minutes to one hour, depending on the completion time of the measurement. One hour of Measurement contains about $30\,\mathrm{GB}$ of data which is a considerable amount for a remotely installed and autonomously running system.

It is important that the gondola, which ascends to the Hafelekar, is not within the line of sight of the radar during measurements. Otherwise, there is a risk of introducing unwanted noise. In particular, this is relevant for the so-called zero measurement. A zero measurement is defined as a measurement conducted with no target or other objects in the line of sight.

4.3. Data processing

In order to generate two-dimensional radar images of the recorded avalanches requires a number of signal processing steps. For a static scenery, the radar data contains intensity over range. For a moving scenery, the changes over time are displayed on a second axis in so-called range-time diagrams or Moving Target Identification (MTI) images. In the following these processing steps are detailed to generate these images.

The processing of the Radar data is done within python. It has robust libraries and tools which offer a powerful platform for digital signal processing and comfortable tools for postprocessing and plotting. A lot of work on the radar data processing has been accomplished by Anselm Köhler. The processing software has matured into an extensive repository of modules, functions, and controlling scripts [22], which is not yet publicly available. The processing stage involves the removal of extraneous data and the application of filters and windows to enhance the quality of the data.

In a first step, the continuous analog signal stream coming from the ADC is chopped into the radar pulses (chirps), which are then rearranged into a two-dimensional dataframe. This is done for the data of mGeodar1 in as a processing step using the additionally acquired marker signal (Figure 2.4) that indicates active chirp pulses. A nice representation of this chirp extraction is shown in figure 7 of Ash et al. (2014) [23]. In the current mGeodar2 version, the triggered acquisition stores the chirp raw data already in such a two-dimensional dataframe.

The crucial step in FMCW radar processing is the transformation from time domain into frequency domain that corresponds to the range according to equation 2.10. This processing of range is achieved by a Fast Fourier Transformation (FFT). Since the input to the FFT needs to be periodic and extendable to infinity a window that tapers the signal to 0 at the edges is required, i.e. it is possible that the signal has not the same level on both edges due to fluctuations in the signal. Typical windows are hamming, blackman or flat-top window [24]. These windows are applied by multiplication with the time domain signal and inhibit frequency sidelobes. However, such a window also reduces the peak of the mainlobe and broadens the mainlobe. Therefore it is possible for the FFT to be misrepresented and the signal cannot be analysed correctly.

Here an arbitrary window the so-called cubic window is applied as can be seen as the black line on the left side in figure 4.2. It resembles a flat top like window with a cubic spline interpolation tapering to the edges. The middle $9\,\mathrm{ms}$ of the $10\,\mathrm{ms}$ chirp stay unchanged. The following code snippet generates the required window with the length `win_len` of 20000 samples.

```
mgeodar.spec.mgeo_spec_window(win_len, parameter = {
    "spec_win_type": "cubic",  # window type
    "spec_win_parameter": 0.05,  #taper over 5% from the sides
})
```

Consequently the data arrays are multiplied with the before mentioned window [25] [24]. In the next step the FFT is used, therefore this code snippet is run.

```
pdspec = pd.Dataframe(np.fft.rfft, axis=1, result_type='expand',
args={parameter['spec_oversampling']})
```

After applying the FFT it is possible to generate the frequency spectrum. With the aid of the before mentioned equation 2.10 and the time delay τ of the received signal, it is possible to execute the range processing. The data is prepared for full range plots by taking the magnitude of the FFT, which is depicted in decibels [23]. The magnitude values are calculated as follows equation 4.1:

$$|z| = \sqrt{a^2 + b^2} \tag{4.1}$$

Where a is the real part and b the imaginary part of the complex number.

The above processing step with the conversion of the time domain chirp data to the amplitude over range data is illustrated in 4.2. The illustration on the left depicts the time domain chirp signal distributed over the entire window, whereas the illustration on the right displays the FFT magnitude in decibels where frequency is already transformed to radar range.

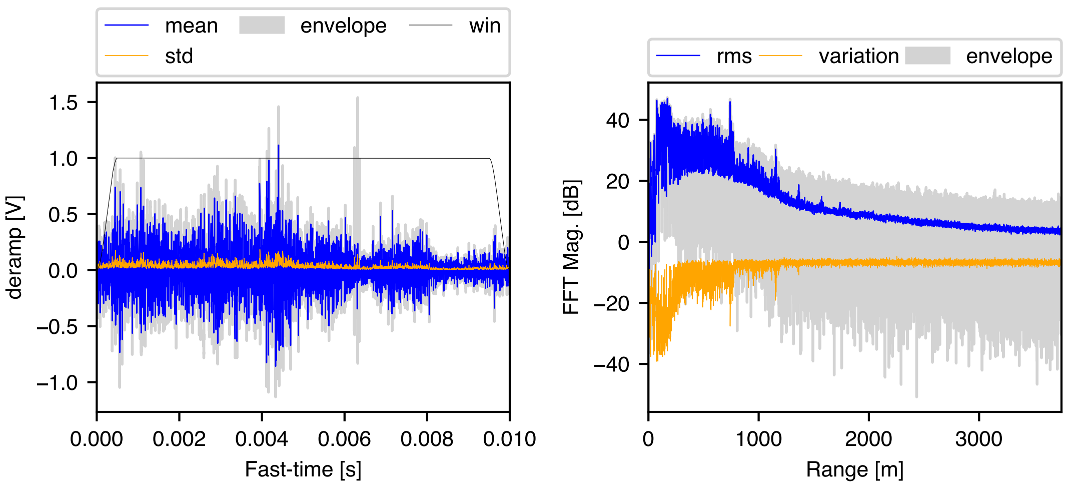

Figure 4.2.: Representation of a chirp with the applied window function (the black line indicated with "win" in the legend) on the left side and on the right side the FFT magnitude in decibel over the range.

On the left side of the plot, the fast-time axis is represented in seconds [s], while the deramp voltage [V] is represented on the y-axis. The duration of the plot is one second. The data series comprises the following elements:

The mean values are represented by the blue line, while the yellow line indicates the standard deviation of the signal. The gray shading marks the envelope with the maximum and minimum values. The black line, labeled "win", shows the window function applied to the signal.

On the right-hand side, the FFT is applied, and the resulting signals are displayed as follows:

Root mean square (rms) values are indicated by the blue line. The variation is represented by the yellow line. The variation is calculated by taking the standard deviation and dividing it by the rms value. The envelope is illustrated with gray lines. This format offers a comprehensive overview of the signal characteristics, presenting both time-domain and frequency-domain analyses.

The background clutter while measuring is high. This can be returns from rocks, dirt in the avalanche path or in case of the Seilbahnrinne the cablecar. These clutters can assume to be stationary throughout the measurement procedure. On that account they can be removed or minimized by using MTI filter. The filters employ coherent subtraction of adjacent sweeps. A detailed description of the fast time processing can be found in following literature [20].

The fast processing ends with the calculation of the range out of the chirp signal from the frequency f. The used equation 2.10 is depicted in section 2.4.1.

It is important to note that the mGEODAR is not capable of detecting an avalanche event in progress. The measurement must be started manually.

Once the data has been preprocessed, a variety of algorithms and techniques can be employed for the analysis of the radar data. The steps are to analyse, transform and visualize the data after the first processing stage.

Therefore Python programming language offers a plethora of libraries and tools that facilitate the efficient completion of these tasks.

The Python Matplotlib library provides sophisticated tools for the creation of plots, maps, and other visualizations, which facilitate the intuitive and informative display of radar data. The data for the $1\,\mathrm{s}$ measurement is visualized as follows: The x-axis represents the range in m while the y-axis depicts the FFT Magnitude in dB. For the longer measurements from $1\,\mathrm{s}$ to $1\,\mathrm{h}$ the x-axis represents the range in m and the y-axis again the FFT magnitude in dB and additionally there is a velocity legend in the right corner which helps to determine the velocity of an avalanche for example in $\mathrm{m\,s^{-1}}$ and an intensity scala on the right side in dB.

The radar data consists out of reflections from the ground, sublayers of the snow, rocks, dirt in the avalanche path or in case of the Seilbahnrinne the cablecar. In general all phenomena that are larger than the wavelength $(\lambda = 37\,\mathrm{cm})$ [12] will give crucial reflections. This background clutter is very high while measuring. As a result, the recorded data is challenging to analyse due to the prevalence of reflections which are within the amplitudes of the reflected signals. The recorded data consists of the background clutter and the actual targets to which the radar is pointing to. These can be snow avalanches, skiers, the gondola or the AT.

After the Fourier transformation the resulting signal describes the intensity in time as a function of distance to the radar device. The chirps of this data are compared to each other and the amplitudes are subtracted. Next the background clutter is erased and only the moving targets are displayed. This is called Moving Target Identification (MTI). The DIFF filter is very short with only 2 samples and has a very soft damping towards the low frequencies.

This MTI filter has 151 samples and a cut-off frequency of $f_c = 0.12$. Additional to the cut-off frequency a low pass filter at a normalized frequency of 0.7 is used to cut out the high frequencies in the end. A sharper frequency response is generated and the low frequencies are reduced while the higher frequency's pass band is flat.

Important to mention is the MTI normalization. For this the mean intensity gives a simple normalization factor. This factor is determined for every data set. Thus the MTI intensities between different avalanches scenarios are difficult to compare. It would be better if the normalization is equal for each dataset recorded with the same radar setup. However to obtain a clean background level, the mean values are calculated in intervals of $5\,\mathrm{s}$ and it is required to have a smooth normalization curve with range. Normalization does not distinguish between upward and downward chirps [14].

This process is called Moving Target Identification (MTI) and first shown in plot 6.10 [3]. Where no movement is visible, the intensity in the plot is around $0\,\mathrm{dB}$ and moving targets with an intensity up to $40\,\mathrm{dB}$.

4.4. Target Calibration

For the target calibration measurements the AT described in section 2.5 is fixed on a tripod to put it in the snow as can be seen in figure 4.1a. Directly close to the AT is a Global Positioning System (GPS) module located to observe the exact position. With the aid of this it is possible to compare radar distance and the actual GPS position. With the aiming scope, the alignment of the AT can be carried out in order to align it directly in sight to the Radar device.

The results of the measurement are presented as described in section 4.3. The top plot illustrates the radar output with the AT on (orange line) and off (blue line). The graph shows a gray area that will be analysed in more detail. The bottom plot shows the differences between the AT powered and AT not powered figure 4.3. And the measurement time is one second.

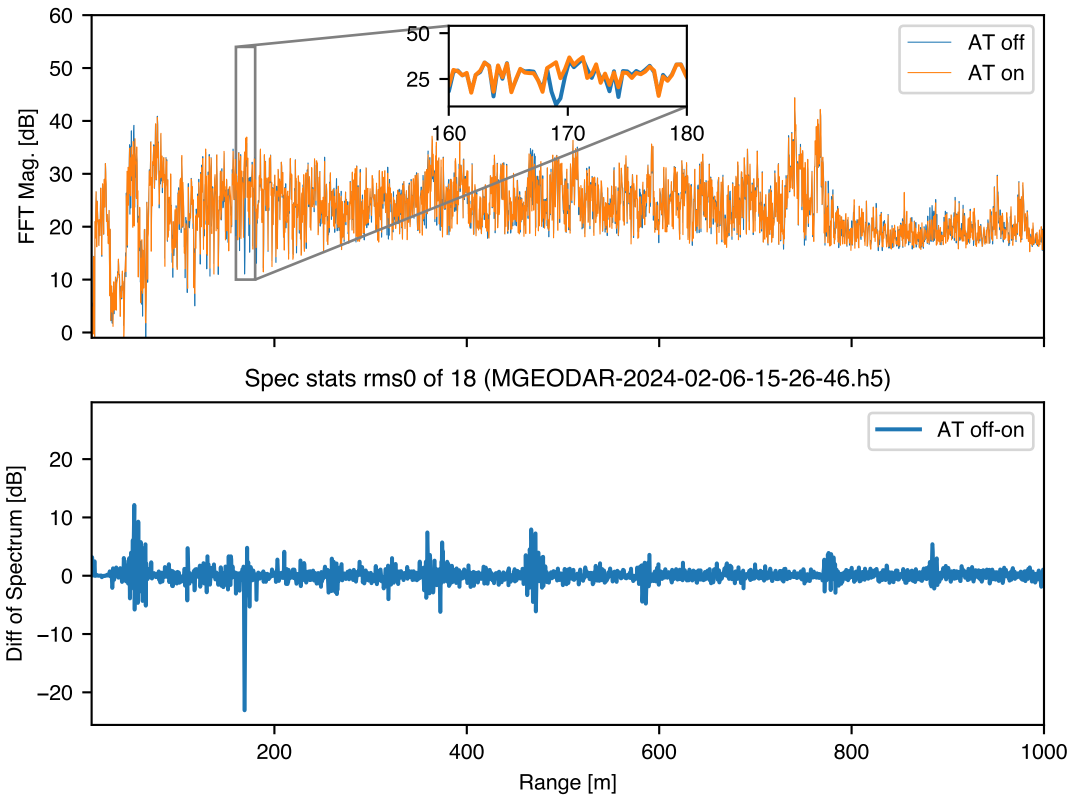

Figure 4.3.: Calibration Measurements with zoomed illustration of the AT position. Upper plot represents zero measurement in blue and target on in orange. The lower plot depicts the difference from target on subtracted from target off.

The gray rectangle shows the area where the AT was located. It is clear that around $169\,\mathrm{m}$ the amplitude where the target was powered is significantly higher than with the AT off. The difference plot also shows a significant peak. Out of this reason the position of the target is clear visible. The comparison with the GPS data shows that the radar range and the GPS distance are matching. The distance between radar device and the GPS dongel where the AT is located, is calculated via the haversine formula. This formula is a very accurate way to calculate distances between points on the surface of a sphere using the latitude and longitude of those points. Because of the reason that altitudes are also included in these measurements, these distances are considered using Pythagoras. In the difference plot there are some additional peaks visible. These can be several factors including the gondola and its counterweight which ascends and descends, people, mirror effects inside the radar, ghost targets and multipath effects (section 6.1.1).

4.5. Radar Calibration

The following illustration 4.4 depicts the elevation pattern of the installed radar transmit and receive antenna *Cobham SA15-90-104V-D1/1124* on the Nordkette.

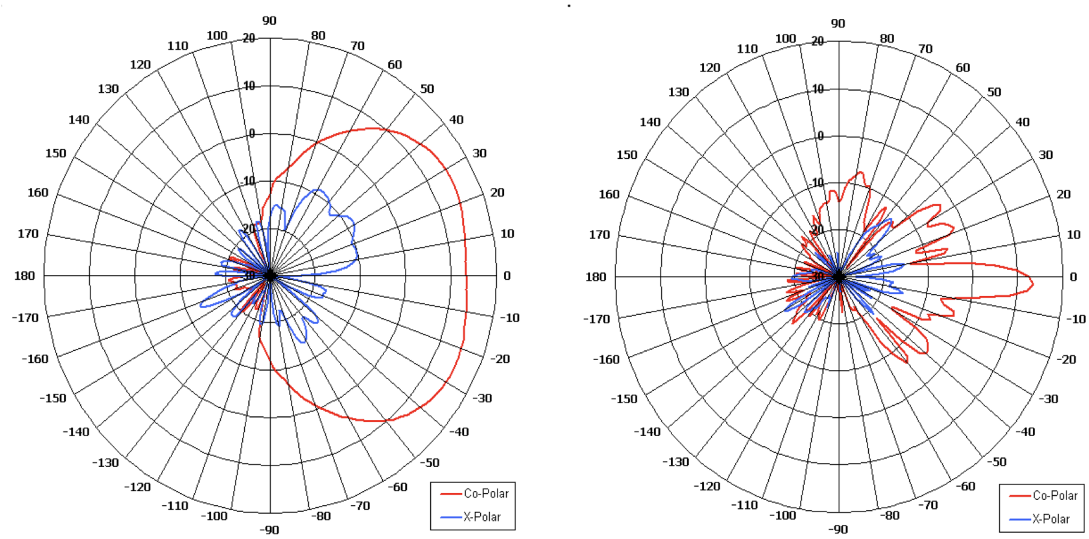

Figure 4.4.: Antenna elevation pattern (left) and azimuth pattern (right) from manufacturer data sheet. Note: The antennas are rotated by $90°$, therefore the azimuth and elevation notations are swapped here compared to the data sheet. Source: `https://www.european-antennas.co.uk/media/1955/ds1124-211010.pdf`

In the plot 4.4 the elevation pattern (left) and azimuth pattern (right) is displayed. The plots display two distinct polarization components: the co-polar (represented in red) and the cross-polar (represented in blue). The relevant one is the co-polar component because the antennas are mounted in a way, that the x-polarization is negligible. In the elevation pattern it is obvious that the opening angle of the co-polar component is from around $\pm 40°$, hence the whole Seilbahnrinne is covered. The azimuth pattern on the right illustrates a cone shape around $\pm 8°$ as the main lobe and some sidelobes of the antenna next to it. The main lobe is clearly pronounced, indicating the primary direction of the antenna's radiation. It extends horizontally around the 0-degree mark, which corresponds to the boresight direction of the antenna. Furthermore, the sidelobes, which are smaller peaks surrounding the main lobe, are visible and indicate unwanted radiation directions that could lead to interference or the detection of false targets. This phenomenon is discussed in the rollmeasurement section 6.4. The cross-polar pattern shows much lower levels of radiation, indicating good polarization purity of the antenna system, which is important for reducing cross-polarization interference and improving signal quality. The elevation pattern provides critical information on the vertical distribution of the antenna's radiation and is essential for understanding its performance in different elevation angles. Hence the opening angle is measured through various measurement points at a distance from AT to radar of around 160 to $170\,\mathrm{m}$. The procedure was conducted in accordance with the instructions depicted in Figure 4.1b. The process commenced at the center of the radar device and proceeded with measurements taken along the right side, returning to the center, and then to the left side. The black circles symbolize the measurement points which are indicated by numbers. With the aid of this it is possible to determine the antenna aperture and viewing direction of the Radar.

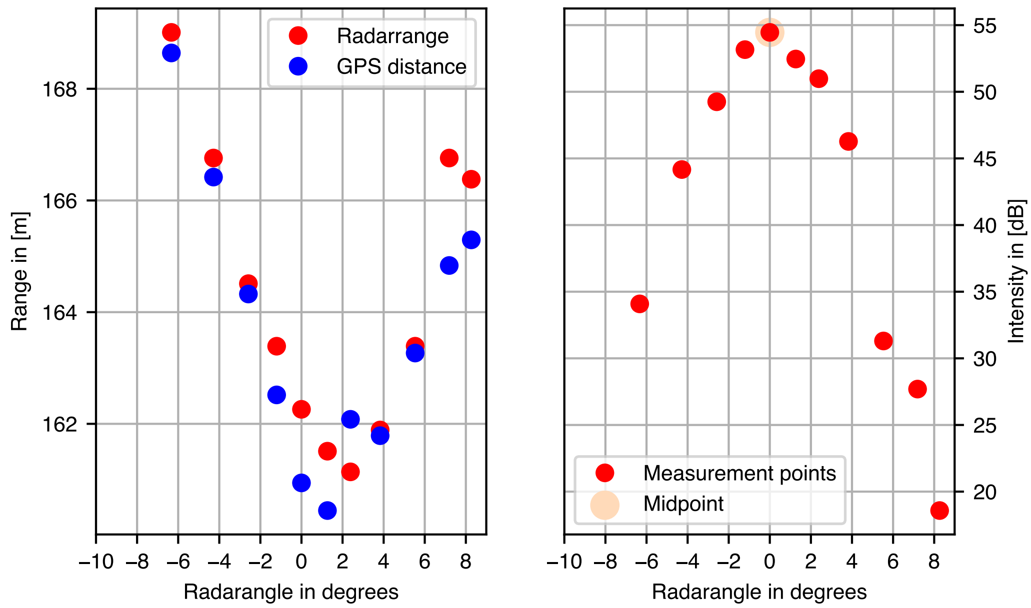

Figure 4.5.: Calibration measurement. On the left side the blue dots representing the radar range and the red ones the calculated GPS range. On the right side the intensity of the target is depicted. Both figures are the same measurement.

Both illustrations in figure 4.5 are representing the same measurement one representation over the range in m and one over the intensity in dB. The data utilized for the calculation may be found in the appendix A, A.1.

The Radarrange in the left plot means the range calculated out of the radar data with the help of formula 2.5 and is represented with red dots and the GPS distance is the calculated distance out of the GPS data and the exact radar position. The figure shows that the GPS and the Radarrange are nearly the same but not identical. The reason for that could be that the GPS data was not calibrated, which means it has an accuracy of only a few meters [26].

Out of the photo 4.1b there is a V-like shape recognizable, this V-shape can also be seen in the figure 4.5 on the left.

Moreover, the plot on the right side illustrates that the intensity of the target is greatest in the middle, with a value of $55\,\mathrm{dB}$. This value is designated as the midpoint and highlighted in salmon color. Outgoing from this value the measurement points to the left and to the right are calculated using the sine of the distances to the midpoint over the vertical distances. As one moves to the right or left, the intensity declines. The lowest point is on the left corner, with a value below $20\,\mathrm{dB}$. This point is also situated outside the 8-degree elevation pattern (figure 4.4), which is the reason why it is not or barely visible in the radar data. It is also evident that the V-shaped profile is oriented downward in this case. Out of figure 4.4 it is obvious that the intensity of the AT diminishes rapidly, as the target is positioned beyond the opening angle ($\pm 8°$), resulting in the emergence of smaller peaks.

5. Realization

5.1. Design of Active Target (AT)

The intention of the design is to utilize the target in field measurements on a tripod setup, as well as to wrap around the concave cubic shape of the AvaNode for measurements inside the avalanche flow [2]. This means the cover needs to be rather durable to withstand the forces in the avalanche. Therefore, an organic mold was developed to minimize sharp edges that are prone to impacts. Therefore a 3D-printed case was designed [27]. This can be seen in figure 5.1. All the necessary items can be accommodated in this component and it can also be used as a field measuring instrument, offering a convenient solution. The batterybox was replaced with a $5000\,\mathrm{mAh}$ power bank, which provides sufficient capacity for one day of pure measurement. The output voltage equals $5\,\mathrm{V}$ which is exactly the needed supply voltage of the amplifier in the AT. The figure 5.1 shows the new target as a field measurement device.

Figure 5.1.: Cover design of AT for field measurements

The AT is designed to be highly practical and user-friendly, making it an excellent choice for field measurements. Its design is optimized for ease of handling, which significantly enhances the efficiency of data collection in various field conditions. The target's portability and ergonomic features contribute to reducing user fatigue, allowing for extended use without compromising performance. Additionally, its robust construction ensures durability and reliability, even in challenging environments.

5.2. Experiment preparation and execution

The following measurements are executed and the results are represented in chapter 6.

Calibration measurements of the radar and the AT are conducted. Accordingly the target will be situated in the avalanche test site, will be executed, including alignment, polarization, distance and orientation measurements. These measurement scenarios are static measurements which means the target is not moving while recording.

The next measurement scenarios are moving measurements. These are roll- and avalanche measurement scenarios. As the name roll measurement implies, it pertains to the AT's rolling motion. The aforementioned measurements were conducted in the following manner: for the initial measurement, the AT was dislodged from the tripod to a distance of approximately $170\,\mathrm{m}$, thereby enabling the desired rolling movement towards the radar to be achieved. For the subsequent measurements, the AT was driven up to the Hafelekar station in order to throw the target from the very top downwards. Thus, insights into the orientation and movement of the target is recorded. Moreover, it provides an inside view into the appearance of the target on radar data, in the event that the AT is rolling down and activated.

For the avalanche measurement on the Nordkette a contingent upon the presence of a minimum fresh snow depth of at least $20\,\mathrm{cm}$ [8]. Without this criterion it is not possible to carry out the blasting. Once the requisite snow depth of $20\,\mathrm{cm}$ has been confirmed, the Avalanche Commission, initiates the blasting operations.

The blasting of the designated area, known as the Seilbahnrinne, marks the commencement of the data collection process. Subsequently, the cube containing the AvaNode (section 1.1) and AT is released into the triggered avalanche following the controlled detonation. As the cube descends with the avalanche, the radar device within continuously gathers essential information. This includes parameters such as avalanche speed, the avalanche path and the length of the avalanche which provide valuable insights into the behavior and characteristics of avalanches. The radar's capacity to monitor the cube's movement within the avalanche ensures the collection of accurate data throughout the event.

6. Results and Discussion

6.1. Characterization of Active Target (AT)

In this section the horizontal and vertical alignment from the AT is analysed. This means the AT is in the line of sight with the radar device. It is rotated from left to right for the horizontal measurement and from upward looking to downward looking for the vertical measurement in two degrees increments. This is done with a compass. The goal of this measurement is to measure the aperture of the AT antenna as they are rather unknown devices. The following plot 6.1 shows the intensity of the AT against the angle alignment.

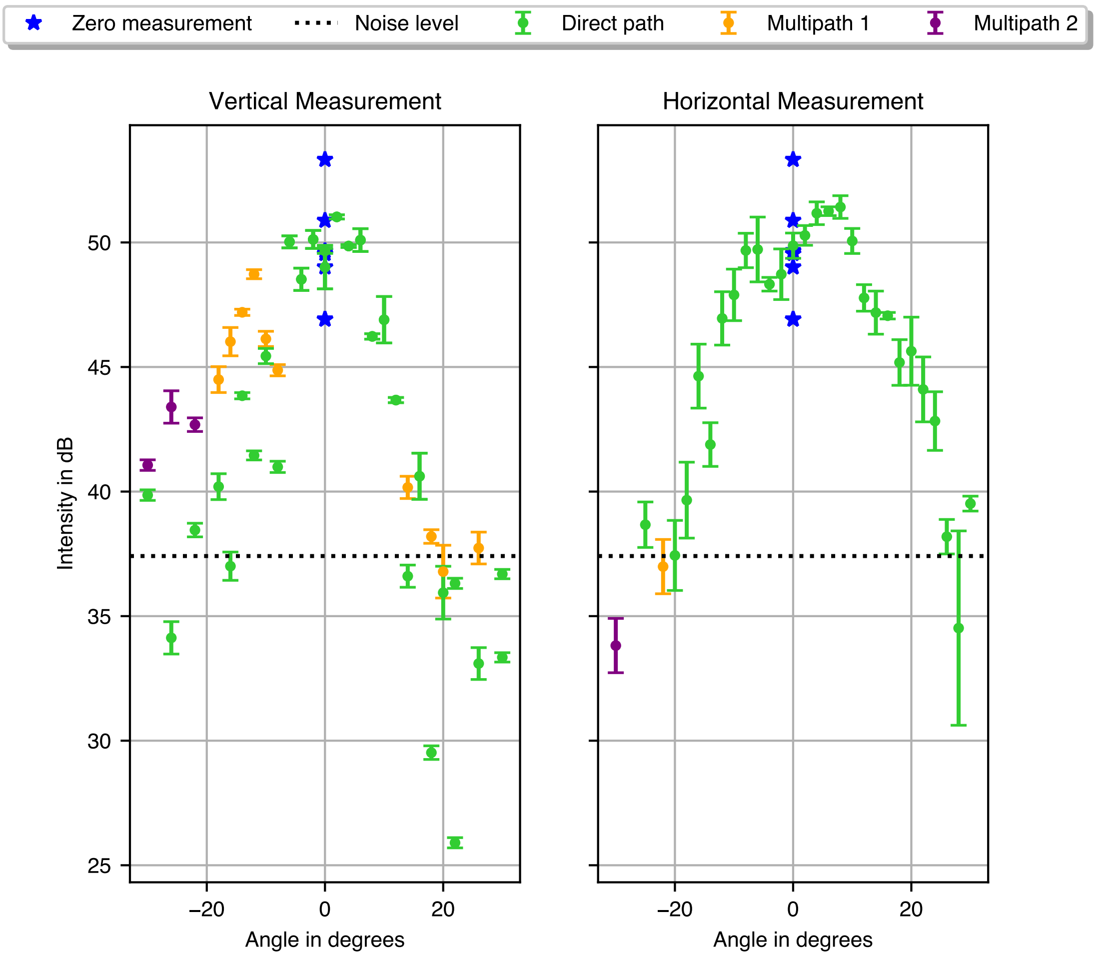

Figure 6.1.: Plots of two different Measurements on the left side the horizontal measurement procedure and on the right side the vertical calibration with error bars can be seen.

The color coding in the two plots 6.1 indicates the following: green represents the direct path, orange the first multipath and purple the second multipath. The blue stars indicate the zero measurements. The error bars show the standard deviation in each measurement point. The black dotted line represents the noise level, which is the mean value of the signals from the no target measurements. Figure 6.1 indicates that the antennas are only functional when oriented from right to left, with a tolerance of plus or minus $20°$.

Out of measured AT antenna pattern A.1 from Novel Wireless Tech the beamwidths of the antenna are around $30°$, which is in close approximation of the measurement results in figure 6.1. The discrepancy is attributed to the dual antenna system which means that there is a specific loss in the receiving antenna and again in the transmitting antenna.

However, values outside an angle of $\pm 20°$ are not valid and below the Noise level (dotted black line). A small dip in intensity is observed around zero degrees. Both the vertical and horizontal measurements exhibit symmetry in the negative and positive angle measurements, forming a bell-like shape with a small central peak.

It is noteworthy that in the vertical measurement (left figure 6.1) a remarkable fidelity to the multipath phenomenon is observable. The green dots (direct path) demonstrate a correlation with the symmetry of the bell-like shape, while the first and second multipath exhibit a greater intensity than the direct path. The multipath will be further elucidated in the subsequent section 6.1.1. It is evident that the phenomenon of multipath is only observable in the vertical measurements (figure 6.1 graph on the left) in the downward direction and not in the horizontal one. This is due to the fact that there are 0 reflections from the sky than from the ground which is covered with snow.

6.1.1. Multipath

As mentioned before the multipath can be recognized in figure 6.1. A Multipath describes when a signal not only propagates directly to the target and back to the radar but also includes additional reflections of objects in the environment [28]. A schematic representation is shown below 6.2.

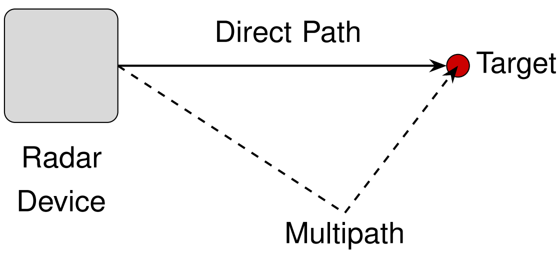

Figure 6.2.: Representation of a radar device with multipath

The diagram 6.2 shows a radar device on the left and the target represented as a red circle on the right. The line represents the direct path from radar to target and the dashed line shows a possible multipath. The illustration provides insight into the existence of additional targets at greater distances. These are called multipath targets [13].

Table 6.1.: Measurement points from left to right in figure 6.1 left side (vertical measurement procedure). Range is the extracted distance of the AT intensity peak from the radar data.

Angle [°]	Amplitude Target on [dB]	Range [m]
-30	41.019359	183.62
-26	43.383179	183.62
-22	42.691765	183.62
-18	44.448767	181.00
-16	45.970101	181.00
-14	47.149768	181.00
-12	48.701711	181.00
-10	46.080403	181.00
-8	44.825158	181.00
-6	50.004148	178.38
-4	48.496056	178.38
-2	50.075474	178.38
0	49.613786	178.38

The table 6.1 describes the vertical measurement procedure therefore the left side of the figure 6.1. The first column of the table enumerates different angles of the target orientation from 0 to -$30°$ in downward direction, while 0 means horizontal alignment of the target. The subsequent columns represent corresponding amplitudes in dB and the belonging range in m.

Upon initial examination, it is evident that there are discernible patterns and trends within the range data. For instance, there are three different range patterns $178.38\,\mathrm{m}$, $181\,\mathrm{m}$ and $183.62\,\mathrm{m}$, where $178.38\,\mathrm{m}$ represents the real distance between target and radar. The other two distances are representing the multipath targets which can be observed in the left panel of figure 6.1 represented by the orange and salmon colors. The multipath of the $181\,\mathrm{m}$ hits the ground in one direction but takes the direct path in the other direction, whereas the $183.62\,\mathrm{m}$ goes over the ground reflection in both directions.

Moreover, by analyzing the data across different categories, several key observations emerge. It is interesting that the intensity of the targets vary between $41\,\mathrm{dB}$ to $50\,\mathrm{dB}$. From the image 6.1 emerges that the intensity values from the multipath are higher than the ones from the direct path. These are caused by the multi-target peaks which occur from the reflections of the signal from the repeater and back [29].

Furthermore, it is important to note any outliers or anomalies within the data that deviate significantly from the general trends. These outliers may warrant further investigation to understand their underlying causes and implications. This is done in the further course of this document in section 6.3 where the focus is to reduce these mirror effects and ghost targets.

6.2. Radar response with range: top to bottom

The measurement procedure were static measurements with the AT from the Hafelekar to the Seegrube station in 10 to $30\,\mathrm{m}$ distances. The goal of this measurement was to get the intensity of the AT with varying range represented in figure 6.3.

The figure 6.3 shows all relevant plots of the top to bottom measurement in sum 34 measurements. On the x-axis is the range from 0 to $1200\,\mathrm{m}$. The y-axis comprises difference plots from AT on and off, which have been normalized from 0 to 1 Viewed From top to bottom the target is situated at a distance of approximately $780\,\mathrm{m}$ for the first measurement point, while at the lowest point, it is located at a distance of approximately $150\,\mathrm{m}$. The green line represents the direct path which can be connected through all the measurements. The line is not straight due to the non-equal spacing of the measurement points. Furthermore, it is evident that there are internal reflections at distances of approximately $207\,\mathrm{m}$ and $412\,\mathrm{m}$ behind the direct signal. These are depicted in salmon and purple colors. In addition there is a vertical mirror effect noticeable. This effect is visible in the lowest plot at around $300\,\mathrm{m}$ up to the eighth plot at around $190\,\mathrm{m}$ indicated by the orange line.

It is crucial to note that the green line was generated by combining the true targets of the difference plots and the salmon and the purple line were simply copied from the green line and moved to the right position. Consequently, it is apparent that these reflections are not mere multipath reflections as observed in section 6.1.1 because the effect in the plot 6.3 always occurs at the same range offset from the original signal. Also ghost targets can be excluded because they typically appear because of side-lobe or multiple reflections while the multipath targets arise from reflections of surfaces and result in the same target appearing at multiple positions [30].

Therefore, the multiple occurring targets are rather hardware-related effects. It is unclear, which part of the radar hardware is able to mirror frequency. Their origin can be internal reflections, aliasing, harmonics or spurious signal which shift their apparent range. An attempt to mitigate these reflections by tuning the radar hardware setting is given in section 6.3.

Figure 6.4 shows the corresponding amplitude intensities to the measurements in figure 6.3. The y-axis represents the amplitude in dB while the x-axis describes the distance from the AT to the radar device in m. The green dots depict the direct targets while the orange and magenta ones are the ghost targets. It is important that the orange dots are in a distance of plus $207\,\mathrm{m}$ and the magenta ones in a distance of $412\,\mathrm{m}$, outgoing from the direct signal. It is plotted this way for the better visualization of the amplitudes of the

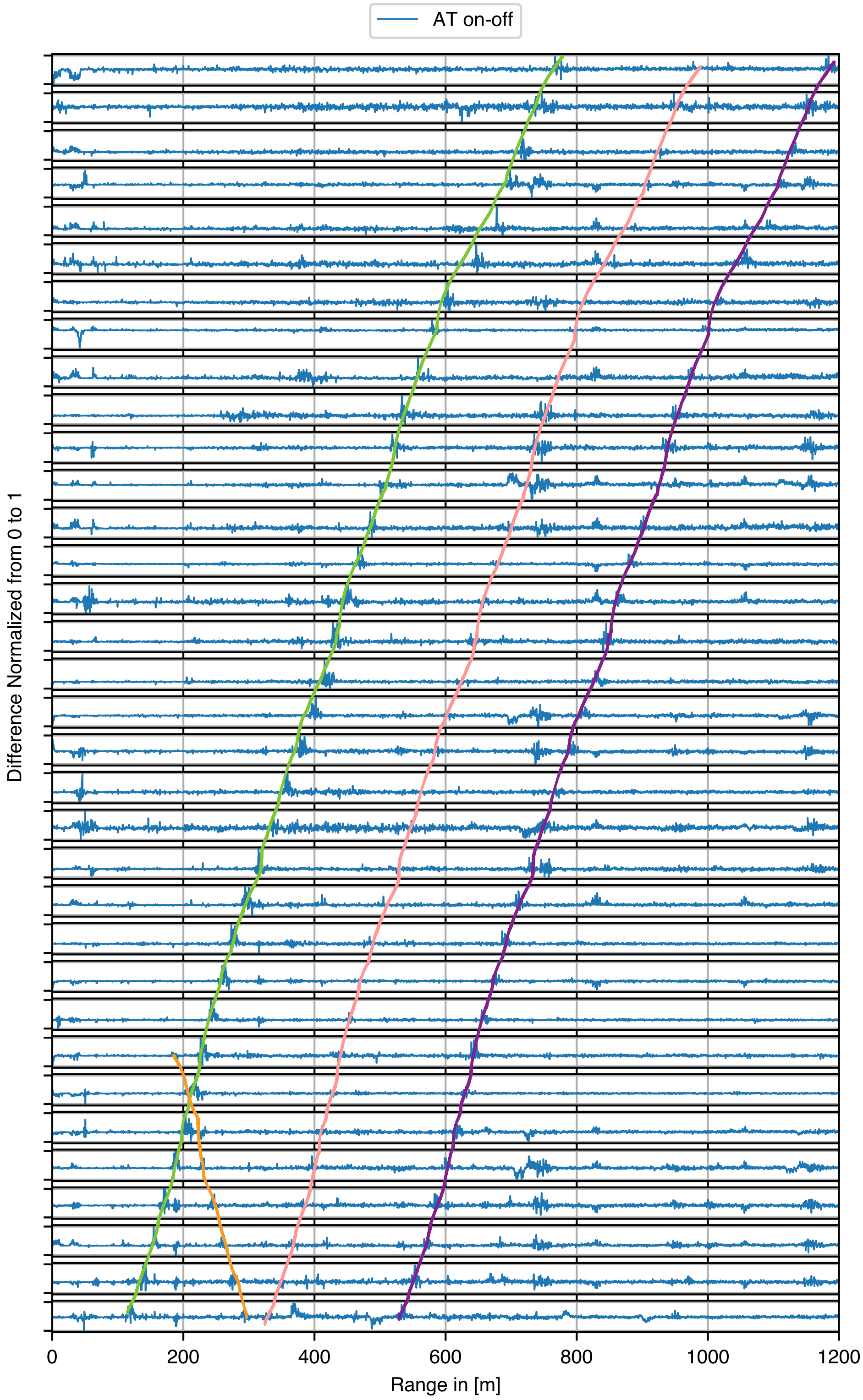

Figure 6.3.: Plot of static measurements in different ranges. The green line represents the true targets and the first and second ghost targets are indicated in salmon and purple respectively. Vertically reflected ghost targets at small ranges are shown with the orange line. Note: The green line is drawn along the true targets while the other lines are copied and shifted to the ghost targets.

true and ghost targets. The true target is at least $10\,\mathrm{dB}$ stronger than the first or second

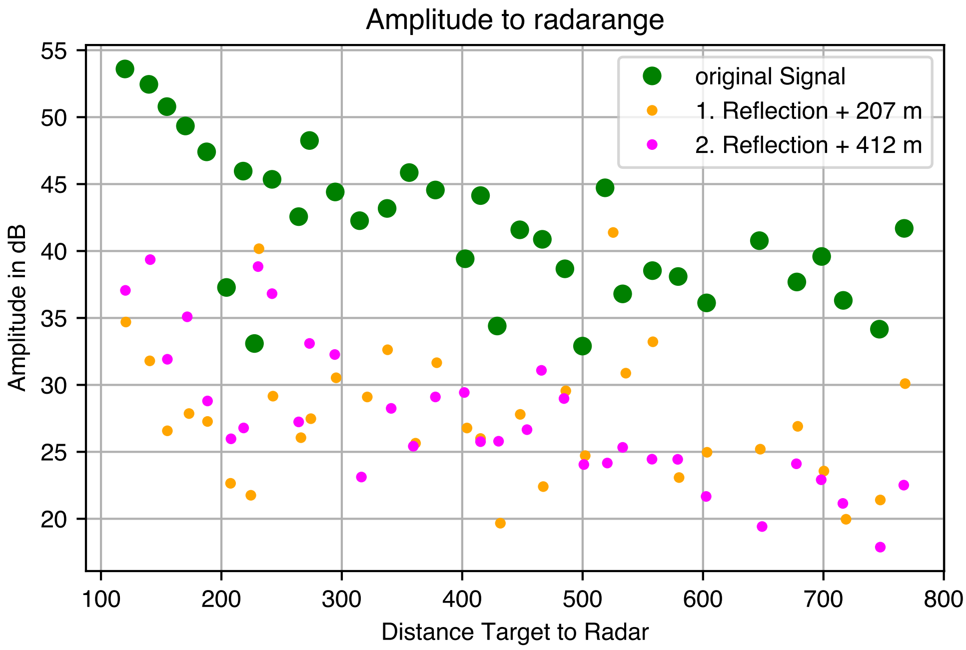

Figure 6.4.: Static measurement from top to bottom, green dots are the direct signal while the orange dots represent the first reflection at the target distance plus $207\,\mathrm{m}$ and the orange dots are representing the second reflection at the target distance plus $412\,\mathrm{m}$.

ghost target.

Normally a range compensation for distance is necessary because the signal strength typically decreases with $1/r^3$. Thus, the baseband filter (section 2.4.2) is used to compensate this range decrease and attenuate the intensity in the closer range of the radar device [12]. This signal strength decrease together with the result of the baseband filter can be seen in the figure 6.4. The signal strength of the AT is relatively constant between $250\,\mathrm{m}$ until $800\,\mathrm{m}$ at $40\,\mathrm{dB}$, but a strongly increases towards smaller ranges indicating that the baseband filter response is not steep enough.

6.3. Radar settings

The aim of this measurement procedure was to change specific radar hardware settings to obtain radar data without or at least with less mirror effects and internal reflections than in the default settings. The default settings were found from laboratory test using a $100\,\mathrm{m}$ long loop cable, but have never been revised in the real world field setting [12]. The results from the previous measurement procedure in section 6.2 show clearly strong reflections at $207\,\mathrm{m}$ and $412\,\mathrm{m}$ range offset from the true target range.

Figure 6.5 represents the radar device in more detail with part numbers for all components. There are three main frequency sections indicated with light gray which are interconnected with up and down conversion mixers in between. Components that are adjustable by software are highlighted with seven purple rectangles.

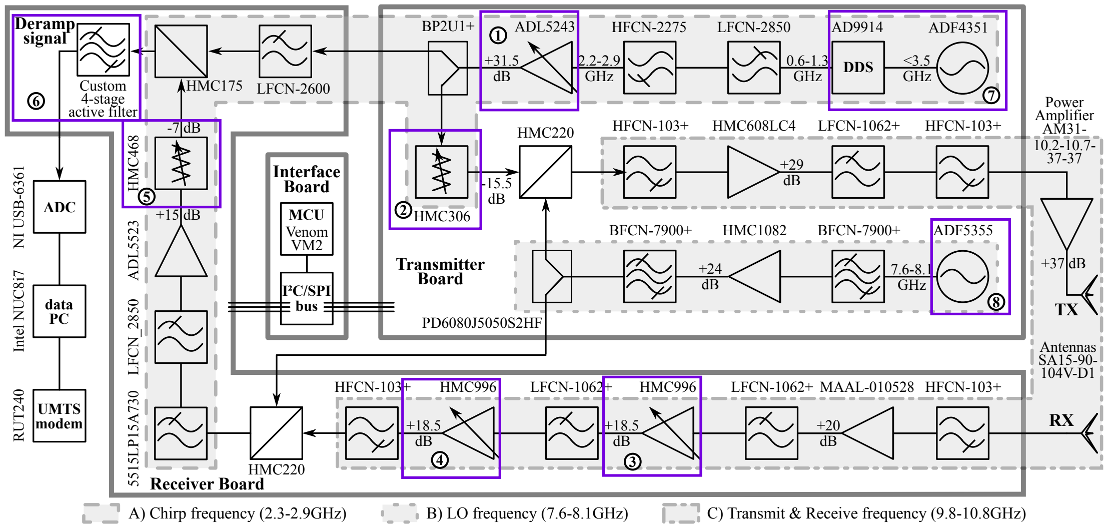

Figure 6.5.: More detailed representation of the mGEODAR hardware. Purple rectangles which are numbered indicate the further inspected configuration opportunities. Reprinted from [12].

These purple rectangles indicate different configuration options in the settings of the mGEODAR radar. 1, 2 are the options for the transmitter chain including an amplifier and an attenuator, respectively. The numbers 3, 4, 5 are for the receiver chain including two amplifiers 3, 4 and also an attenuator 5. The custom 4-stage active filter, which is the baseband filter is marked with number 6. Item 7 is for the configuration of the DDS chip to generate the chirp signal, which also dependent on the clock source (ADF4351). And item 8 is another local oscillator which together with the DDS results in the desired high-frequency output signal of $10\,2$ to $10.6\,\mathrm{GHz}$.

Following avalanche measurement figure 6.6 is analysed. The avalanche was recorded on the 25.01.24 at 10:36 o'clock.

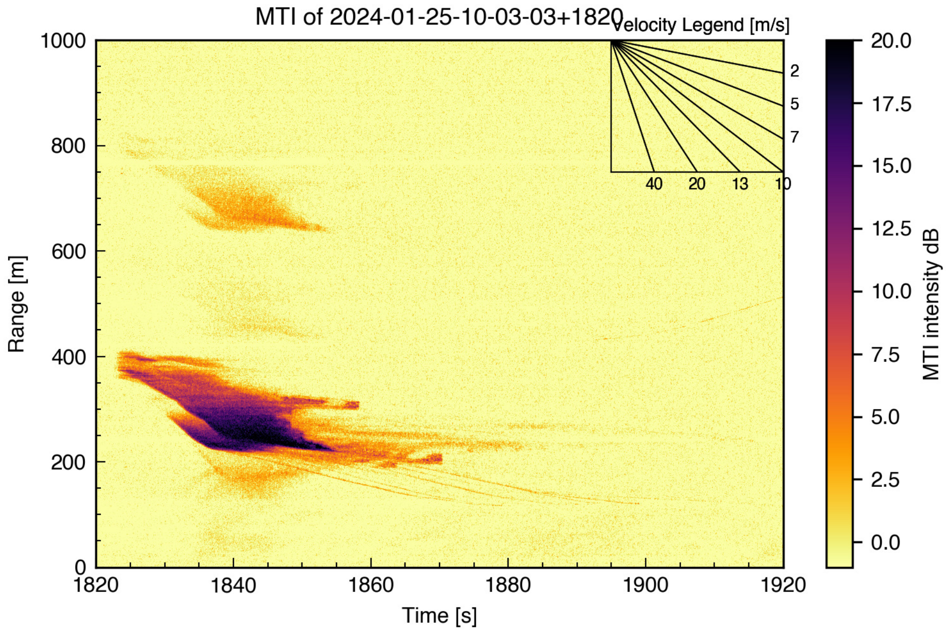

Figure 6.6.: Avalanche scenario with ghost targets from the 25.01.24 at 10:36 o'clock.

It is noteworthy that the avalanche descended from a distance of 400 to $160\,\mathrm{m}$ radar range. Small snowballs were observed emanating from the avalanche, visible as small orange stripes in the range of 200 to $100\,\mathrm{m}$ at a time between $1840\,\mathrm{s}$ and $1900\,\mathrm{s}$. The intensity level of the avalanche is around 5 to more than $20\,\mathrm{dB}$. Above the avalanche is the first ghost target detectable with very low signal starting at a range of $450\,\mathrm{m}$ and a time of around $1840\,\mathrm{s}$. The second ghost target is more pronounced at a radar range of $800\,\mathrm{to}\ 650\,\mathrm{m}$ starting at around $1825\,\mathrm{s}$. It is worthy to mention that the mirror effects only occur when the intensity level of the target is above $15\,\mathrm{dB}$, which is herein called an over amplified target as discussed later in section 6.4. The ghost targets appear at a range of $+207\,\mathrm{m}$ and $+412\,\mathrm{m}$ to the real target as mentioned before in section 6.2.

For the reason that only strong intensity signal result in reflections, three measurement scenarios which changes settings in transmitter chain, receiver chain and baseband filter are depicted. The first measurement point P1 in figure 6.7 is the difference plot for the default settings which are:

Table 6.2.: Default settings of the baseband filter, receiver chain and transmitter chain for the radar device A.3

Baseband (Nr. 6)	Receiver (Nr. 3–5)	Transmitter (Nr. 1–2)	Point number
10|24|0.1|6	16.0|16.0|0.0	27.9|-4.5	1

The formats for the various configurations and their respective locations are indicated by the accompanying number in the figure 6.5.

- Baseband (Nr. 6) contains 4 filter stages: Stage1 | Stage2 | Stage3 | Stage4 [12]

- Receiver chain: Amplifier (Nr. 3) | Amplifier (Nr. 4) | Attenuator (Nr. 5)
- Transmitter chain: Amplifier1 (Nr. 1) | Attenuator (Nr. 2)

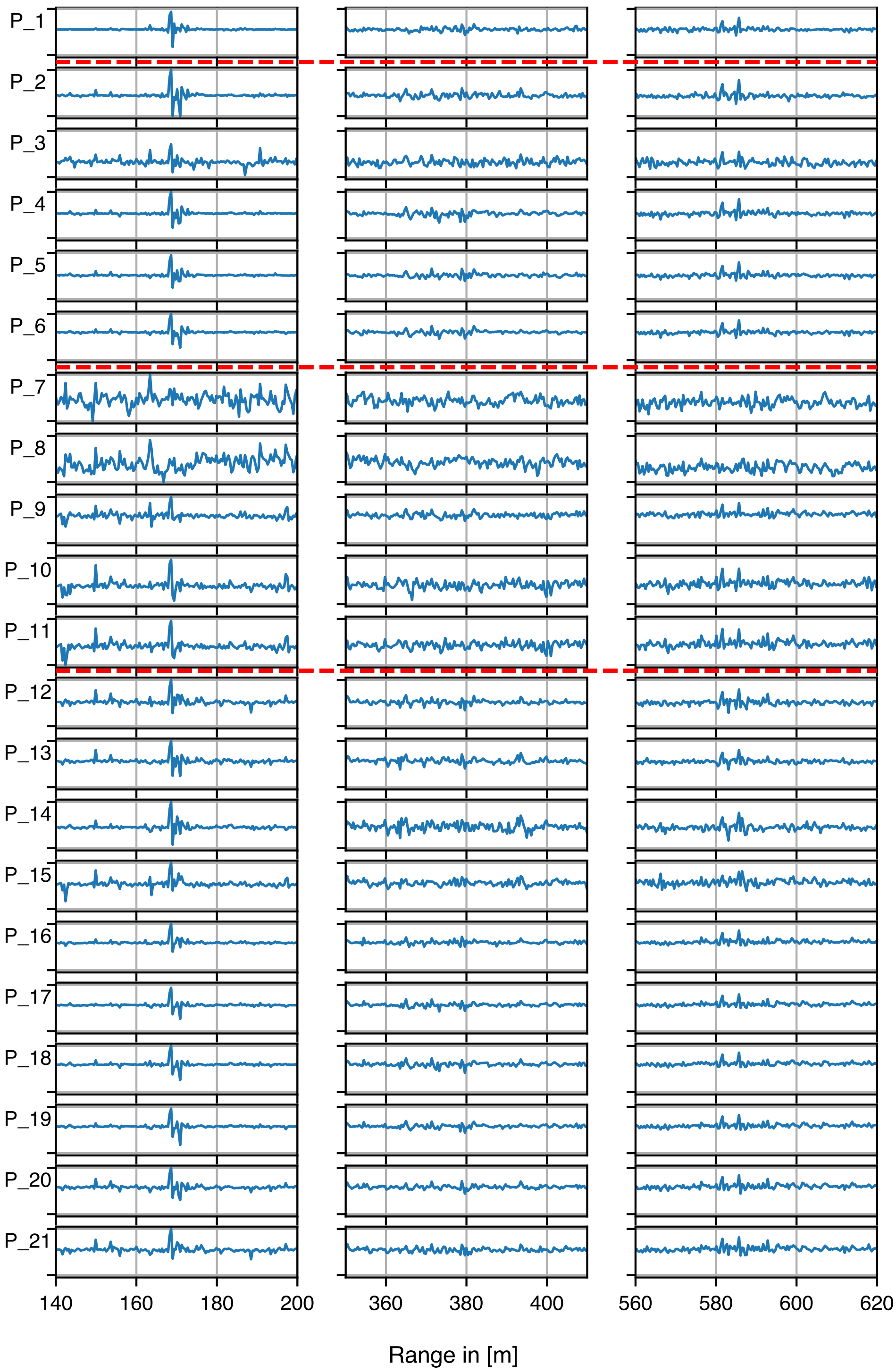

Figure 6.7.: Radar settings in three different ranges to highlight the mirror effects outgoing from the main target at a radar range of $170\,\mathrm{m}$. The red dashed lines symbolize the change in the radar settings. Therefore first point is the default settings measurement. P2 to P6 are changes in the baseband filter stages, P7 to P11 are settings in the transmitter chain and P12 to P21 are settings in the receiver chain.

In figure 6.7 the three different radar settings measurement scenarios are represented.

The exact listing of the changed radar setting parameters can be found in the appendix table A.3. The blue line in the plot depicts the difference between a zero-measurement using the default settings and a measurement with the AT activated but using different setting parameters. This plot is split in three areas with the red dashed lines. P1 shows a measurement in the default settings. The second area includes P2 to P6 with changes in the baseband filter stages, the third P7 to P11 with changes in the transmitter chain and P12 to P21 with changes in the receiver chain. It is split in three columns for different range segments. The AT is always located at a distance of around $170\,\mathrm{m}$. In the first one the range segment is from 140 to $200\,\mathrm{m}$ and give therefore the direct signal. The second range segment from 350 to $410\,\mathrm{m}$ and the third one from 560 to $620\,\mathrm{m}$ illustrate only the ghost targets of the true target in the first column. On the y-axis there are again the normalized values from 0 to 1 and the P's describe which point at which measurement scenario which can be found in the appendix in table A.3. It is interesting that the third column shows a double mirror peak, while the target comprises only a single significant peak. The signal in the second column is often not discernible from the noise, as the much lower intensities are also indicated in figure 6.6 at a range of $500\,\mathrm{m}$ and with the salmon line in figure 6.3.

6.3.1. Mirror effects and 4-stage baseband filter

In following measurements the settings for the baseband filter are changed. It is implemented as four stage active bandpass filter. Peak gain frequency is around $430\,\mathrm{kHz}$ or $1600\,\mathrm{m}$ range. Simulated response of the baseband filter for high and low gain response can be found in the mGEODAR hardware paper [12].

The measurement points P2 to P6 symbolize changes in the baseband filter. Due to the over amplified targets above $20\,\mathrm{dB}$, which can be observed in Figure 6.6, the objective of this measurement was to reduce the intensity level to the point where a ghost target is no longer visible. As can be seen in Figure 6.7, the radar settings have undergone some changes, yet the double peak at approximately $580\,\mathrm{m}$ persists. For point P2, the lowest settings for the baseband filter (10|12|0|-6) are used, but the AT is still clearly observable, as is the double peak in the third column. Point P3 has the highest settings (21|24|10|6), which indicates that the baseband filter attenuates the received signals most. Upon examining the 4-stage baseband filter at its highest settings, it becomes evident that the majority of the signal is filtered out, resulting in a notable similarity between the noise and signal. Consequently, the Signal to Noise Ratio (SNR) is not a reliable indicator in this context.

Thus, the AT is indistinguishable from different signals and the double peak is obscured by the noise. The subsequent three points, P4, P5 and P6 are situated midway through the baseband filter stages. There are no serious changes in the difference-plots, e.g. the difference between a zero-measurement with default settings and a AT measurement with the corresponding baseband filter setting. Consequently, the target is once again discernible, accompanied by the double peak in the third column. It can be posited that modifying these settings is not the optimal approach for avoiding this mirror effects, because it reduces mainly the SNR values and for example weak avalanche signal will be lost with stronger baseband settings.

6.3.2. Changings in receiver and transmitter chain

Points P7 to P11 illustrate different transmitter chain settings, while the points P12 to P21 display different receiver chain settings. In the initial measurement, point P1, the AT is clearly visible at $170\,\mathrm{m}$ with the default settings in table 6.2. It is notable that the second column exhibits only minor visible ghost targets at approximately $380\,\mathrm{m}$, while in the third column, the double peak is observable at $583\,\mathrm{m}$.

P7 and P8 exhibit a weak transmit chain with an amplifier (1) gain of 22.9 and $16.9\,\mathrm{dB}$, respectively, while the default transmit amplifier has a gain of $27.9\,\mathrm{dB}$, which precludes the appearance of the AT at all and only noise is shown. SNR is again not visible for those points. Additionally, the small peak in the middle column and the double peak in the third column is similarly affected, rendering it undetectable. Therefore these settings are in this use case unwanted. After lifting the amplifier (1) gain in the transmitter chain from measurement point P9 on, the target at $170\,\mathrm{m}$ and the double peak at $583\,\mathrm{m}$ become visible again. Also the attenuator value is changed from 0 to -9 in points P9 to P11 which results in a damped signal of the transmitter chain.

In the subsequent measurement process, the receiver chain is altered from points P12 to P21. These measurements demonstrate minimal differences. If the transmitter chain's gain is insufficient, the difference between noise and the actual target becomes undetectable. The disappearance of the double peak in the third column is not achieved through changing values in the receiver chain. The AT is evident in every measurement point except points P7 and P8 where the transmitter chain gain was too low. In the range area from 350 to $410\,\mathrm{m}$ the light ghost target remains at $380\,\mathrm{m}$ and the double peak mirror effect at $585\,\mathrm{m}$ stays also nearly the same.

6.3.3. Spurious signals

Hence, even with modified the signal strength, the desired elimination of the mirror effects remains unattained. These mirror effects give rise to a number of other reasons and namely the problem of spurious signals [31]. Many active high-frequency components are prone to have discrete noise spikes at discrete frequencies, mostly known as harmonics that are integer multiples of the operating frequency. However, those noise spikes can also occur at other frequencies and are then commonly called spurious signals. These spurious signals, including harmonics, have always smaller signal intensities than the operating signal, the amplitude difference is the spurious free dynamic range.

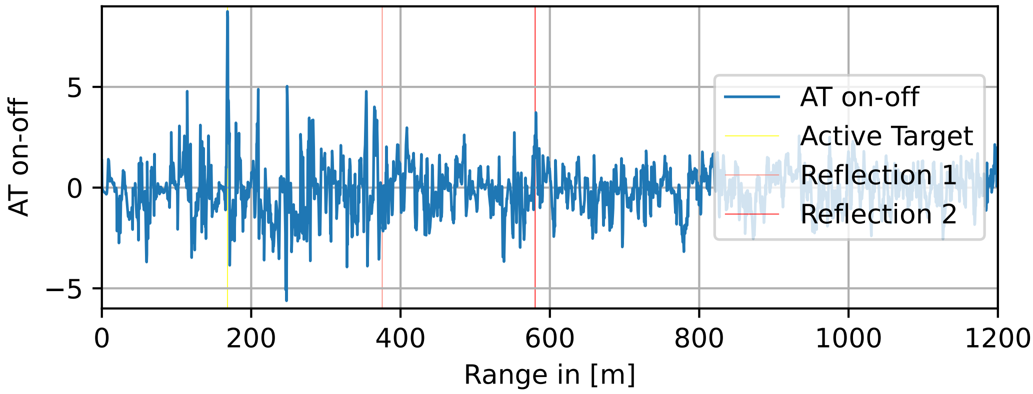

Figure 6.8.: Difference plot for measurement with changes in the DDS and Local Oscillator settings.

The signal generation scheme for mGEODAR radar is composed of a DDS (7) together with a Local Oscillator (LO) (8) and with an up conversion mixer results in the desired transmit frequency (figure 6.5). While the modification of the baseband and transmitter / receiver settings mainly focused on balancing the amplitude between the different frequency sections in the radar hardware, i.e. making optimal use of the spurious free dynamic range. The following paragraph tunes the DDS and the LO to a slightly different frequency region and therefor hoping to shift the spurious signal.

The default settings for the LO, the clock and DDS are $8.12\,\mathrm{GHz}$, $3.48\,\mathrm{GHz}$ and a linear chirp from $2.08\,\mathrm{GHz}$ – $2.48\,\mathrm{GHz}$, respectively. For the test to move the spurious signals, the settings for the LO, the clock and DDS are modified to $7.88\,\mathrm{GHz}$, $3.7\,\mathrm{GHz}$ and a linear chirp from $2.32\,\mathrm{GHz}$ – $2.72\,\mathrm{GHz}$, respectively. The idea was to change the high-frequency setting of every signal source, since every signal source can be origin for spurious signals.

Figure 6.8 shows the difference-plot between a measurement with target off and target on for the full radar range. The main signal of the AT is a nearly $9\,\mathrm{dB}$ above the zero measurement. The second reflection is still visible at $580\,\mathrm{m}$, but with $6\,\mathrm{dB}$ it is not the strongest spurious signal. Many more spurious signal appeared in between $200\,\mathrm{m}$ and $400\,\mathrm{m}$, potentially, because the chirp data with these settings is not flat and unbalanced between lower and upper end of the chirp ramp. In this case the signal distribution of the chirps occupies only one-third of the length compared to the relatively balanced chirp signals in the default settings as shown figure 4.2. Unfortunately, the main outcome of this test settings is that the strong ghost target at $+412\,\mathrm{m}$ did not disappear. So potential spurious signals of the frequency sources – DDS, clock and LO – are not the cause for the ghost targets and their origin mirror effect stays unclear.

6.4. Roll Measurements

This measurement procedure describes the AT rolling down the Seilbahnrinne at the Nordkette towards the radar. There are two different Measurement types which are described in the following.

In contrast to all previous results which focus on static measurement, this dynamic set up requires a different method to display the data. The MTI filtering as previously mentioned in section 4.3.

Those MTI plot have the x-axis with time in s and y-axis with radar range in m. The plot does not always start from $0\,\mathrm{s}$ because normally the Radar data acquisition is started before the actual measurement to be sure that everything is recorded properly. Such range-time diagram enables to estimate an approach for the velocity of a target. In the right corner of the illustrations there is a velocity Scala in $\mathrm{m\,s^{-1}}$ which enables to estimate the speeds towards the radar but not necessarily a ground parallel speed. The colorbar scala on the right represents the intensity in dB from -5 to $40\,\mathrm{dB}$. A normalization at times when nothing is moving in the dataset reduces stationary background scatters to intensities between -5 to $5\,\mathrm{dB}$. Moving targets have typical intensities in the range from 5 to $25\,\mathrm{dB}$. As later explained, the measurement here also include targets with unusual high intensities between 25 and $40\,\mathrm{dB}$.

The first measurement describes a roll measurement covering about $70\,\mathrm{m}$ of rolling distance of the cube. The procedure took place from $190\,\mathrm{m}$ to $120\,\mathrm{m}$ range from the radar to the AT. The picture 6.9 shows a measurement procedure from the 21.02.24 at 12:11:30. In the picture the orientation of the radar device is depicted with black lines. The red line symbolizes the path of the rolling AT. The circle number one is the starting point of the AT. Circle two describes the AT at the current time T = $97\,\mathrm{s}$. Circle 3 and 4 indicate the presence of ski touring persons. The person depicted in circle 3 is within the radar's field of view, while the other one is outside the field of view of the radar device.

The radar data of the measurement is shown in figure 6.10 with the range-time MTI plot. For the background normalization the first $8\,\mathrm{s}$ of the measurement are used. The magenta colored dashed line indicates the time point of the shown webcam picture at $97\,\mathrm{s}$. The rolling target is the diagonal line from $190\,\mathrm{m}$ to $120\,\mathrm{m}$ range and between $87\,\mathrm{s}$ to $110\,\mathrm{s}$. Also the two ski touring individuals at a range of $100\,\mathrm{m}$ to $110\,\mathrm{m}$ are moving during the measurement over the full time span, and occasionally me moving slightly during the measurement at a range of $190\,\mathrm{m}$ are visible in the radar data. It is noticeable, that one ski touring person (circle 3 in figure 6.9) is reflecting with a high intensity of 25 to $40\,\mathrm{dB}$ at $110\,\mathrm{m}$ even though he remains stationary. It is visible in the webcam video, that he is constantly moving with his hands and sometimes the whole body. The second person (circle 4 in figure 6.9) is most of the time outside the viewing angle of the radar. He starts moving from $97\,\mathrm{s}$ till $105\,\mathrm{s}$ and constantly progresses into the radar field of view from $108\,\mathrm{s}$ onwards.

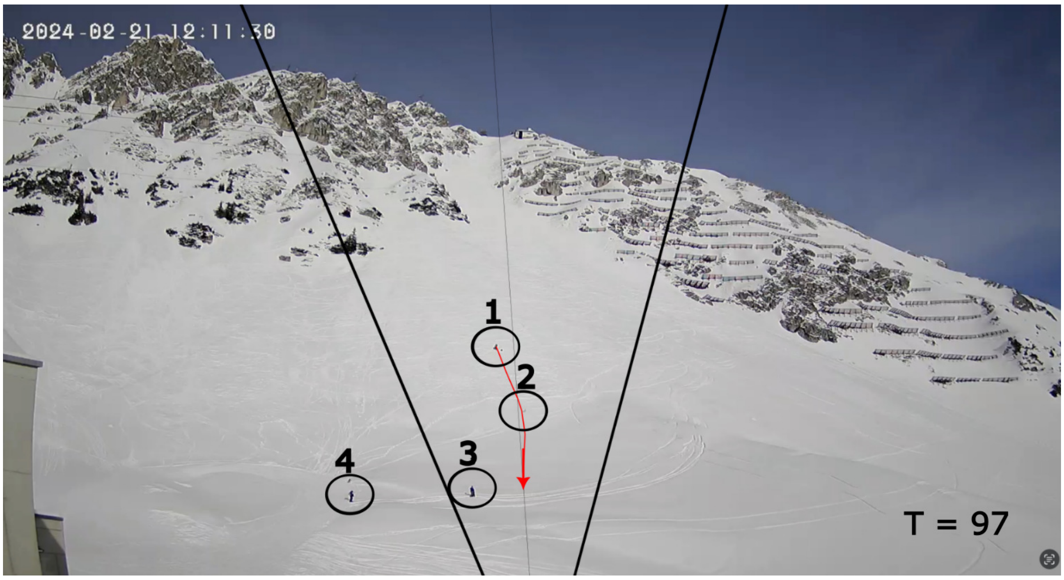

Figure 6.9.: Webcam picture in operation direction of the radar device at the Nordkette at timestamp t = $97\,\mathrm{s}$ Picture with radar cone and roll measurement process.

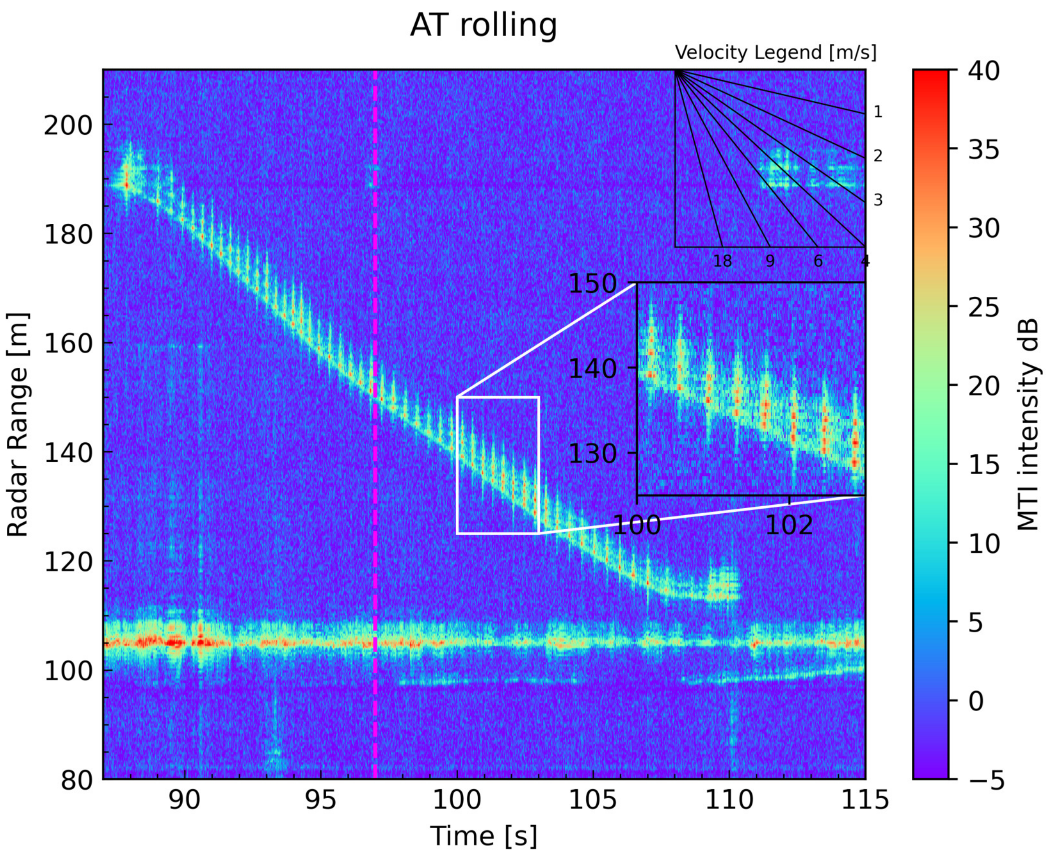

Figure 6.10.: Rolling target within the testside in a range from about $190\,\mathrm{m}$ to $120\,\mathrm{m}$. Magenta colored dashed line indicates time when the picture in Figure 6.9 was taken.

The AT exhibits high intensities of approximately up to 30 - $40\,\mathrm{dB}$. The zoomed inset, indicated with the white rectangle at a distance of $125\,\mathrm{m}$ to $150\,\mathrm{m}$ and 100 to $103\,\mathrm{s}$, displays the rolling AT. Interestingly, the target appears with regularly spaced repeating peaks in intensity. The speed can be estimated to approximately $4\,\mathrm{m\,s^{-1}}$, which is derived from the velocity legend. The recurring peaks indicate the rotation of the target, as the orientation of the AT to the radar is very important, as previously stated in section 4.1, figure 4.1a. The peaks have an interval of approximately $0.4\,\mathrm{s}$. This distance between the bottom of consecutive peaks is approximately four range bins which equals $4 \cdot 0.37\,\mathrm{cm} = 1.48\,\mathrm{m}$. Taken the dimensions of the cube of $30\,\mathrm{cm}$ by $40\,\mathrm{cm}$ gives a total length of $1.4\,\mathrm{m}$ for a complete rotation.

It is evident that the peaks are distributed over several meters in range with multiple small intensity peaks, e.g. at $102\,\mathrm{s}$ are three small red peaks and for the next occurrence are five red peaks visible.

The reason for this phenomenon remains unclear, but several possible effects can cause such spreading or widening of a single target. A first possibility can be due to the Doppler effect, as the range in equation 2.4 is influenced by velocity. However, the target exhibits a similar spread in the y-direction throughout the entire process, including the stationary phase from $108\,\mathrm{s}$ onwards. Therefore it is highly unlikely that the Doppler effect can be attributed here.

A second reason could be spectral leakage [32] during the processing of the radar data and the estimation of frequency, that relates to range in equation 2.10. Such spectral leakage can appear because of applying window functions which introduce sidelobes, or ripples, to the spectral density of the signal [24]. However, even when testing different window function prior to taking the FFT, the AT signal stayed spread across multiple ranges.

Another explanation can be the before mentioned multipath effect in section 6.1.1. This effect could cause the multiple intensity peaks. In section 6.1.1 are the discovered distances between multipath and real path between 2 and $3\,\mathrm{m}$. This is approximately the same distance which can be seen in the highlighted area as the red intensity peaks.

A more severe possible explanation for the spectral spreading could be internally in the radar hardware. Since the AT shows such unusual high intensity about 30 to $40\,\mathrm{dB}$, it is possible that certain components in the receiver chain are saturated which can cause a wide spread of the intensity over several frequencies and thus over several ranges. The high signal intensities can be therefore called over amplified intensities. The receiver chain consists basically of two mixers and some amplifiers to balance the signal levels. Due to the build of the radar on printed circuit boards, it is close to impossible to measure the signal in the receiver chain and therefore it is very difficult to rule out this possible explanation. Needless to say, the AT is a good method to identify such problems, and future repeats of these measurements could involve changing internal radar parameters as it has been done in the laboratory in [12].

A comparison to the measurements with the AT, the very same trajectory as the rolling cube was travelled by human walking towards the radar. The photo in figure 6.11

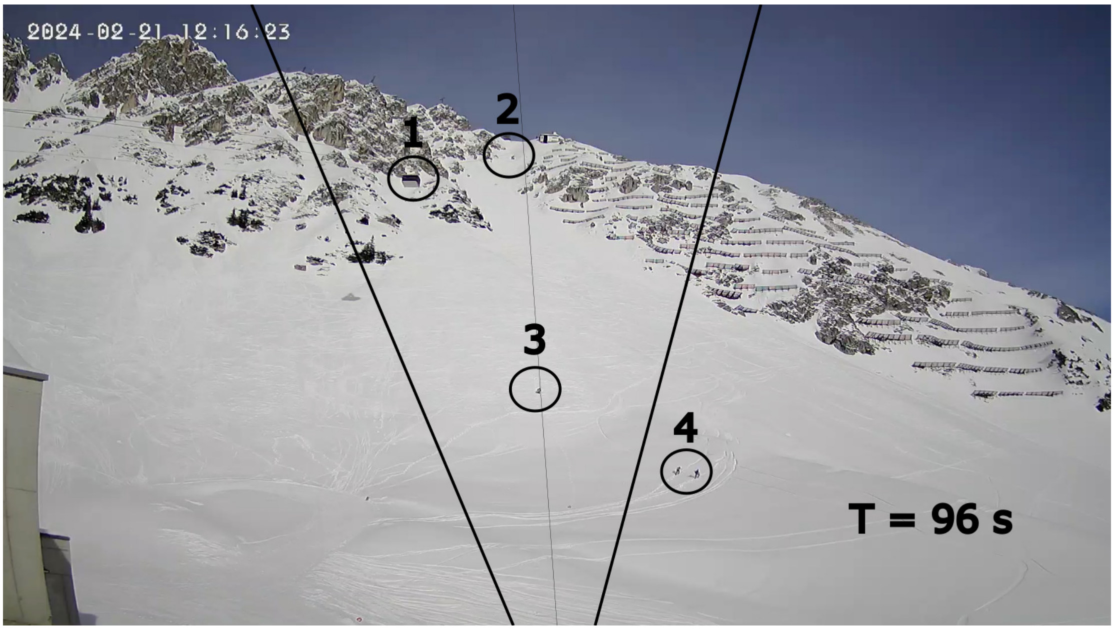

Figure 6.11.: Webcam picture in operation direction of the radar device at timestamp T = $96\,\mathrm{s}$.

visualizes this scenario from the 21.02.24 at 12:16:23 o'clock. The illustration indicates the Gondola with circle one, the counterweight with circle two, the human walking towards the radar device with circle three and the two ski touring persons with circle four.

Figure 6.12 shows the range-time plot of the measurement scenario similar to the roll measurement previously described. One can see a high intensity level from $190\,\mathrm{m}$ to $110\,\mathrm{m}$, human walking. The magenta colored dashed line symbolizes the webcam timestamp of $96\,\mathrm{s}$ out of the previously mentioned picture 6.11.

On the left side, starting from $118\,\mathrm{m}$ and moving uphill away from the radar, another weak target is visible. This target consists of the two touring individuals who are moving uphill. Both are outside the operating area of the radar device at the timestamp of $96\,\mathrm{s}$ (black cone-shaped lines in figure 6.11).

The oblique stripe in figure 6.12, which starts at $76\,\mathrm{s}$ from the bottom, indicates the gondola's ascent. Initially, the gondola is outside the operational range of the radar device, which results in its disappearance and reappearance. This occurrence can be observed in the time period of 76 to $86\,\mathrm{s}$ at a range of 80 to $140\,\mathrm{m}$. This is due to the aforementioned radar pattern figure 4.4. Where the gondola traverses the sidelobes of the antenna pattern, where the intensity levels fluctuate between a minimum and a maximum which causes appearing and disappearing. The counterweight of the gondola, with a somewhat less pronounced characteristics, is observable at approximately $155\,\mathrm{s}$, slightly above the human walking at a range of $150\,\mathrm{m}$ and again at $160\,\mathrm{s}$ till $165\,\mathrm{s}$ at a range of $100\,\mathrm{m}$ to the bottom. It exhibits a similar disappearing and reappearing effect as the gondola which is also caused by the antenna pattern. The three vertical stripes starting at $90\,\mathrm{s}$, $119\,\mathrm{s}$ and $121\,\mathrm{s}$ represent skiers who are within the operational radar range at this time point and are responsible for the vertical interference. The reason for

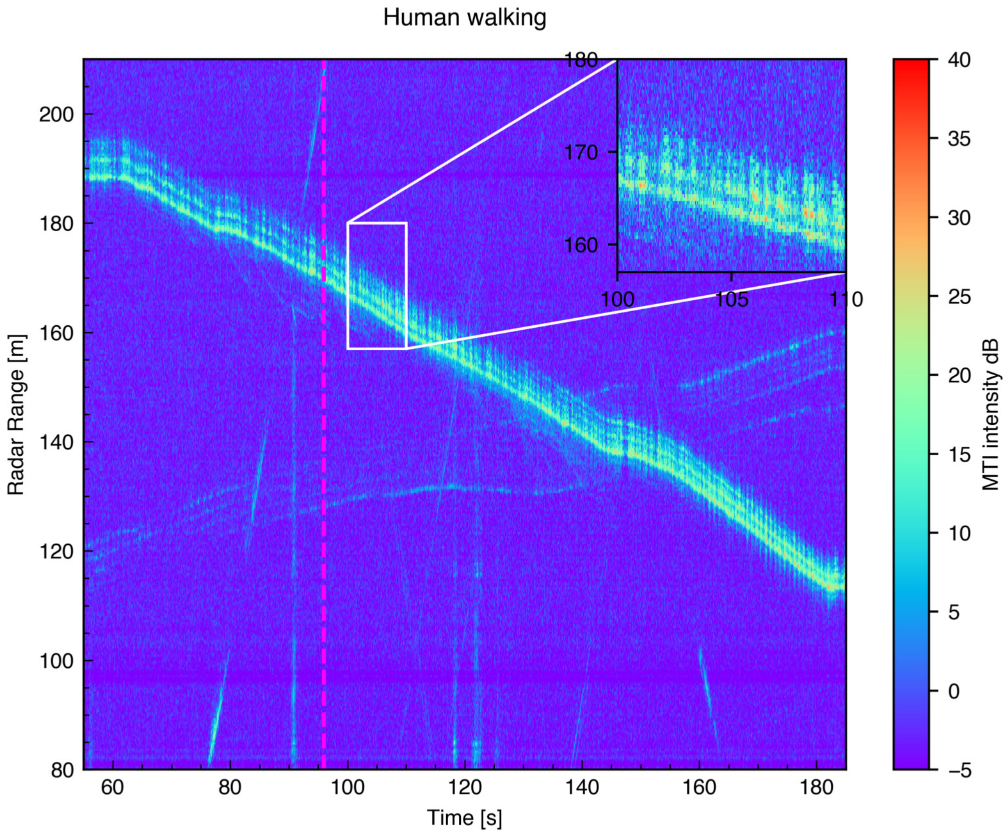

Figure 6.12.: Human walking towards the radar device. Magenta colored dashed line indicates time when the picture in Figure 6.11 was taken.

this could also be the aforementioned saturation of components in the receiver chain of the radar.

A more detailed analysis of the human walking in figure 6.12 reveals a number of interesting characteristics. As illustrated, a person is approaching the radar device within the operational area of the radar. However, the image appears as three stripes in the illustration. The zoomed area of the plot, indicated with the white rectangle, provides a more detailed depiction. It can be observed that the intensity is partially over amplified. The three stripes could also be attributed to the previously mentioned spectral leakage and multipath phenomena. It is also noteworthy that while the individual is walking, some small snowballs are rolling down, which can be seen as weak targets in the plot.

6.5. Avalanche Measurement with Active Target (AT)

The following chapter represents an avalanche measurement from the 20^{th} of February 2024. The FMCW radar is pointing as mentioned before figure 2.2 towards the Seilbahnrinne and the recording of measurement data started at 07:33:31. The blasting for the Seilbahnrinne was initiated at 8:12. Thus $38\,\mathrm{min}$ and $48\,\mathrm{s}$ after the start of recording which corresponds to $2328\,\mathrm{s}$. At this point in time the avalanche is triggered. In next figure 6.13 the avalanche is visualized within the target is located and the GPS data is recorded.

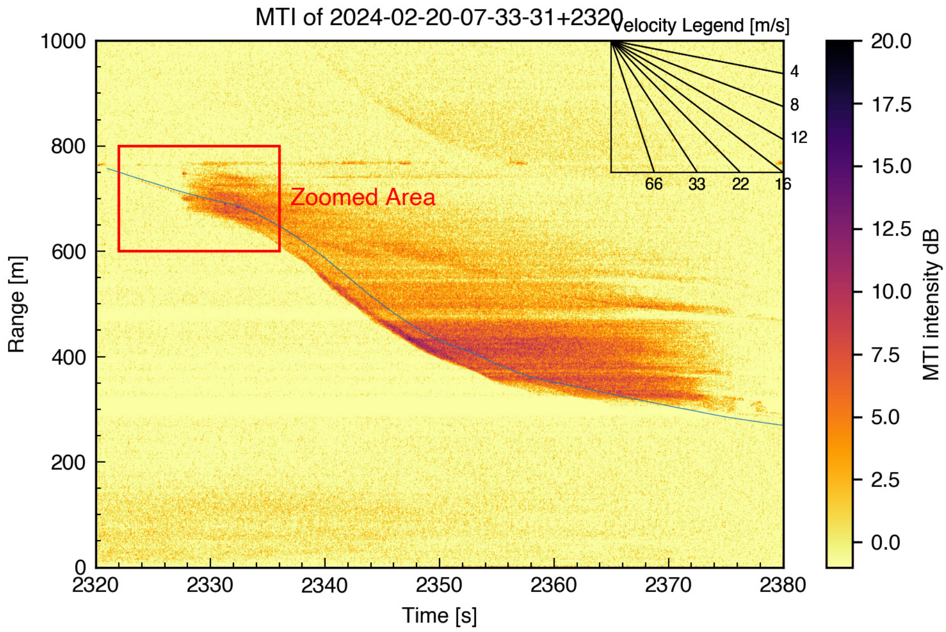

Figure 6.13.: Avalanche with AT and GPS validation. GPS data equals the blue line and the avalanche is indicated with the orange color in the plot starting at a time point of around $2330\,\mathrm{s}$.

As displayed in the previous plots from the section 6.4, this plot displays the range in m on the y-axis and the time in s on the x-axis. The occurrence of the avalanche is clearly visible in the center of the plot, resulting from a change in intensity caused by the MTI filtering. The orange coloration indicates a heightened intensity, which is a consequence of the avalanche in the radar data. The avalanche started at a radar range from about $750\,\mathrm{m}$ and descended to approximately $300\,\mathrm{m}$ in a time window of $50\,\mathrm{s}$. The ghost target in a range of $+412\,\mathrm{m}$ is also visible at a timestamp of $2340\,\mathrm{s}$ to $2365\,\mathrm{s}$. Inside this avalanche the AT is recognizable at the upper part of the avalanche in the region of $750\,\mathrm{m}$ to $650\,\mathrm{m}$. The red rectangle indicates the zoomed area which is represented in the figure 6.14 below. The GPS data clearly demonstrates that the AT follows the path of the avalanche and even has the same speed as the avalanche itself. In the initial section extending from $750\,\mathrm{m}$ to $650\,\mathrm{m}$ the velocity of the cube and avalanche amounts to $4\,\mathrm{m\,s^{-1}}$. Subsequently the velocity increases to approximately $15\,\mathrm{m\,s^{-1}}$ until $500\,\mathrm{m}$. From there on both entities exhibit a deceleration, reaching a velocity of around $4\,\mathrm{m\,s^{-1}}$. The avalanche remains at a distance of $300\,\mathrm{m}$ after nearly $50\,\mathrm{s}$ while the measurement cube continuous to roll down with the speed out of the viewed plot. Considering the Zoomed area in the next illustration 6.14 which is indicated with the red rectangle in figure 6.13 again.

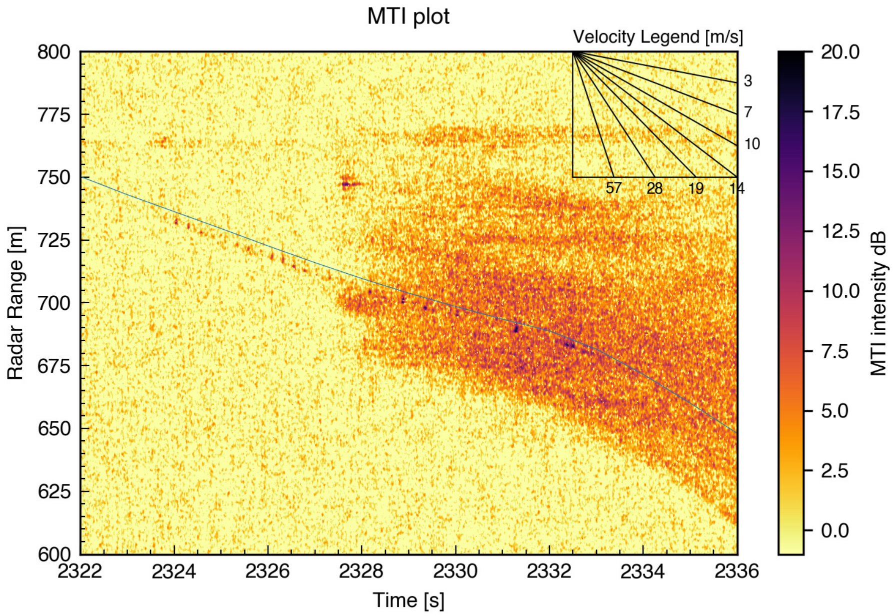

Figure 6.14.: Zoomed area of the upper part from the avalanche. Noticed with a red rectangle in figure 6.13. The recurring peaks indicate the AT in the beginning of the avalanche scenario and the blue line imply the GPS data.

The plot has the same units on the axis as the plots before. But the considered radar range is from $600\,\mathrm{m}$ to $800\,\mathrm{m}$ and the time from 2322 to $2336\,\mathrm{s}$.

It is immediately apparent that there are again the repeated peaks in intensity which could be seen in the roll measurements figure 6.10 from $730\,\mathrm{m}$ to $680\,\mathrm{m}$. These occurrences are representing the AT.

It is perceptible that the radar data and the GPS data has a small offset. This offset comes of a time offset. The time in the GPS is recorded in one second steps which leads to small uncertainties. Furthermore the GPS data is not atmospheric corrected which causes a systematic error. This means that the location accuracy is limited to 3 to $5\,\mathrm{m}$.

After $680\,\mathrm{m}$ the AT is not visible anymore. The reason for that could be that the cube is under a too thick layer of snow, the power supply has an interruption or the antenna cable became loose. Nevertheless the target is visible in the beginning and the in-flow sensor can be directly synchronized with the radar data which previously had to rely on simultaneous clocks [2]. Consequently the trajectory of the synthetic particle can be traced with great precision and with the reference of the overall avalanche that the radar image provides.

6.6. Comparison between snow- and synthetic particle

At the 19^{th} of April 2024 another small cornice avalanche was triggered. The special about this avalanche situation is that there is no measurement device inside. The process can be seen in illustration 6.15.

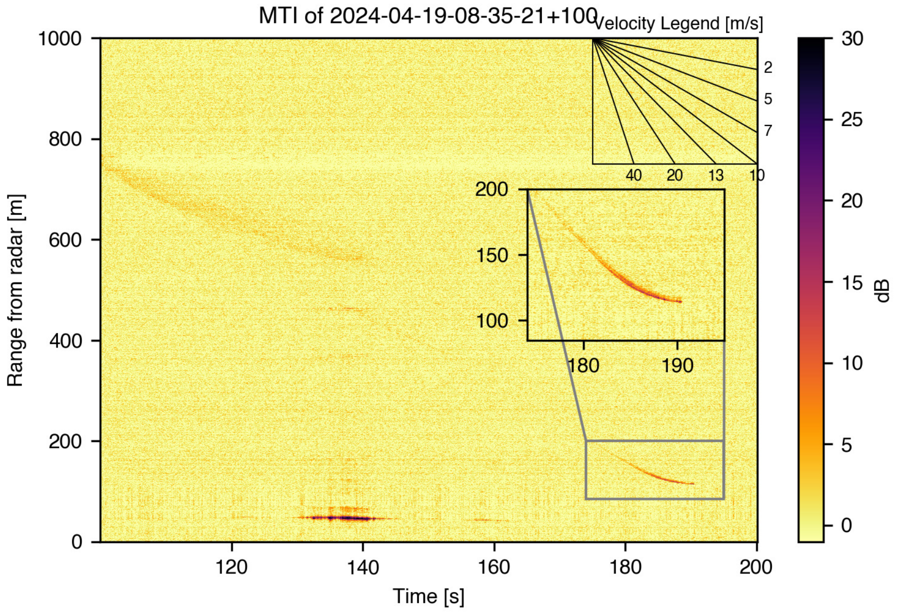

Figure 6.15.: Cornice Blasting from the top of the Nordkette

The intriguing aspect of this phenomenon is that a small snowball, situated at a distance of approximately $200\,\mathrm{m}$ and $175\,\mathrm{s}$, is observed to be in motion. The gray rectangle depicts the snowball in a magnified illustration. This leads to the conclusion that the target exhibits a similar structure to that of a snowball which has been triggered by an avalanche.

7. Conclusion

The objective of this thesis includes the development and tracking of the AT in an avalanche scenario and using this AT in various measurement scenarios, such as calibration, roll and avalanche measurements to improve the mGEODAR radar performance.

The development and functionality of the AT, along with its calibration using the mGEODAR radar, are successfully accomplished. The AT operates effectively for all relevant ranges, when oriented within $\pm 20°$ along the line of sight of the radar. The signal strength of the AT is sufficient for measurements at all relevant ranges of the mGEODAR radar and indicates the baseband filter as effective.

Existing avalanche measurements reveal mirror effects in the radar hardware that cause ghost targets to appear at consistent range offsets and are investigated through calibration measurements. Multiple radar settings are tested to vary the baseband filter, the receiver and transmitter chain as well as the high-frequency signals sources. Although problematic ghost targets persist as shown in figure 6.6, they only occur when targets are over amplified, typically within $300\,\mathrm{m}$ of the radar range. These over amplified targets additionally exhibit spectral leakage, causing their detected location to spread over several meters.

The combination of radar technology with the AT and an in-flow sensor acting as a synthetic particle proves effective. It is possible to track the AT inside an avalanche enabling synchronization between in-flow sensor data and radar data.

Using an AT with a radar device represents a significant advancement, providing a known reference target for field measurements and simplifying the use of complex radar devices. Despite these advances, challenges remain. Multipath effects, environmental factors, snowpack variability, and hardware issues can hinder measurement accuracy. Careful calibration and ongoing adjustments are necessary and an AT is an ideal tool.

In conclusion, the gained insights from roll and avalanche measurements, the calibration of the radar system by applying various radar settings have improved the understanding of the radar device mGEODAR. Further improvements of the AT include shape adjustments or the use of omnidirectional antennas. Future research should continue exploring these technologies to enhance precision and applicability in other tracking applications.

Bibliography

[1] J. Schweizer, J. B. Jamieson, and M. Schneebeli, “Snow avalanche formation,” *Reviews of Geophysics*, vol. 41, no. 4, 2003. doi: 10.1029/2002RG000123

[2] M. Neuhauser, A. Köhler, R. Neurauter, M. S. Adams and J.-T. Fischer, “Particle trajectories, velocities, accelerations and rotation rates in snow avalanches,” *Annals of Glaciology (IGS)*, 2023. doi: 10.1017/aog.2023.69

[3] N. M. Vriend, J. N. McElwaine, B. Sovilla, C. J. Keylock, M. Ash, P. V. Brennan, “High-resolution radar measurements of snow avalanches,” *Geophysical Research Letters*, 2013. doi: 10.1002/grl.50134

[4] A. Köhler, J. N. McElwaine, and B. Sovilla, “Geodar data and the flow regimes of snow avalanches,” *Journal of Geophysical Research: Earth Surface*, vol. 123, no. 6, pp. 1272–1294, 2018. doi: 10.1002/2017JF004375

[5] D. G. Long, A. Brummer, and B. Nalli, “Microwave radar system for detecting avalanches,” *Proceedings, International Snow Science Workshop, Breckenridge, Colorado*, 2016. [Online]. Available: https://arc.lib.montana.edu/snow-science/item/2286

[6] S. Harvey, “Lawinenarten,” Accessed: 17.05.2024. [Online]. Available: https://www.slf.ch/de/lawinen/lawinenkunde-und-praevention/lawinenarten/

[7] X. Li, B. Sovilla, C. Jiang, J. Gaume, “Three-dimensional and real-scale modeling of flow regimes in dense snow avalanches,” *Landslides*, 2021.

[8] H. Müller, “Lawinensprengungen auf der Nordkette in Innsbruck,” Accessed: 10.03.2024. [Online]. Available: https://www.innsbruck.info/blog/de/sport-natur/lawinensprengungen/

[9] “Das Telemobiloskop,” Accessed: 13.05.2024, Daidalos. [Online]. Available: https://www.daidalos.blog/innovationen/meilensteine/artikel/telemobiloskop/

[10] M. Skolnik, *Radar Handbook*, 3rd ed. The McGraw-Hill Companies, 2008. ISBN 978-0071485470

[11] H. Gubler and M. Hiller, “The use of microwave fmcw radar in snow and avalanche research,” *Cold Regions Science and Technology*, vol. 9, no. 2, pp. 109–119, 1984. doi: 10.1016/0165-232X(84)90003-X

[12] A. Köhler, L. B. Lok, S. Felbermayr, N. Peters , P. V. Brennan , and J.-T. Fischer, “mGEODAR – a mobile radar system for detection and monitoring of gravitational mass-movements,” *Sensors*, October 30, 2020.

[13] J.-J. Lin, Y.-P. Li, W.-C. Hsu, and T.-S. Lee, "Design of an FMCW radar baseband signal processing system for automotive application," *SpringerPlus*, vol. 5, no. 1, p. 42, 2016. doi: 10.1186/s40064-015-1583-5

[14] A. Köhler, "High resolution radar imaging of snow avalanches," Dissertation, Durham University, 2017. [Online]. Available: http://etheses.dur.ac.uk/12556/

[15] Z. Zahra, "Stimulation eines Radar-Objekterkennungs- und Trackingverfahren mit synthetischen Daten," Master Thesis, Technische Universität Darmstadt, 2020.

[16] Analog Devices, "AD9914," Accessed: 11.04.2024. [Online]. Available: https://www.analog.com/media/en/technical-documentation/data-sheets/ad9914.pdf

[17] S. Felbermayr, "Scheckkartencomputer-basierte Datenerfassung für ein mobiles Lawinenradar," Bachelor Thesis, Management Center Innsbruck, 2020.

[18] T. W. Ping Li, "Power consumption model construction and analysis for soft synchronization FMCW radar," *IEEE Access*, 2016. doi: 10.1109/ACCESS.2023.3311265

[19] B. N. Möhring, "Frequency-modulated continuous-wave radar for tracing discontinuities on transmission lines," Dissertation, Technische Universität München, 2023.

[20] M. J. Ash, "FMCW phased array radar for imaging snow avalanches," Dissertation, University College London, 2012.

[21] M. Winkler, "Vergleich von AvaFrame-Lawinensimulationen mit mGeodar-Radarmessungen am Beispiel von gesprengten Lawinen auf der Nordkette," Master Thesis, Universität Innsbruck, 2022.

[22] A. Köhler, "Code repository," Accessed: 15.02.24. [Online]. Available: https://bitbucket.org/snowavalanche/fmcw_processing/src/master/

[23] M. J. Ash, P. V. Brennan, C. J. Keylock, N. M. Vriend, J. N. McElwaine, B. Sovilla, "Two-dimensional radar imaging of flowing avalanches," *Cold Regions Science and Technology*, 2013.

[24] S. W. Smith, *The Scientist and Engineer's Guide to Digital Signal Processing*, 2nd ed. California Technical Publishing San Diego, California, 1999.

[25] T. J. Horst, "Radarbasierte Hinderniserkennung für einen autonomen Quadrocopter," Bachelor Thesis, Universität Würzburg, 2015.

[26] K. S.-N. and A. S. Fotheringham, "Calibrating spatial interaction models from gps tracking data: An example of retail behaviour," *Computers, Environment and Urban Systems*, vol. 74, pp. 136–150, 2019. doi: 10.1016/j.compenvurbsys.2018.10.005

[27] N. Haberstroh and A. Köhler, "3D print design for mgeodar active target cover," *Zenodo*, 2024. doi: 10.5281/zenodo.12801962

[28] F. Bischeltsrieder, M. Peichl, and W. Utschick, "On dispersion and multipath effects in harmonic radar imaging applications," *MDPI*, December 9, 2021. doi: 10.3390/rs13245013

[29] D. Werbunat, “Ghost-target,” *Universität Ulm*, 2016.

[30] G. E. Smith and B. G. Mobasseri, “Multipath exploitation for radar target classification,” in *2012 IEEE Radar Conference*, 2012. doi: 10.1109/RADAR.2012.6212215 pp. 0623–0628.

[31] A. W. Doerry, D. L. Bickel, “Discriminating spurious signals in radar data using multiple channels,” *Sandia National Laboratories*, 2012.

[32] N. Tomen, J. C. v. Gemert, “Spectral Leakage and Rethinking the Kernel Size in CNNs,” *Computer Vision Lab, Delft University of Technology*, 2021.

List of Figures

List of Tables

List of Acronyms

AT Active Target

GPS Global Positioning System

Radar RAdio Detection and RAnging

FMCW Frequency Modulated Continous Wave

RX Receiver Antenna

TX Transmitter Antenna

ADC Analog-to-Digital Converter

PC personal computer

DDS Direct digital synthesis

FFT Fast Fourier Transformation

MTI Moving Target Identification

IMU Inertia Measurement Unit

GNSS Global Navigation Satellite Systems

wlan WLAN
Wireless Local Area Network

BFW Austrian Research Center for Forests

SNR Signal to Noise Ratio

LO Local Oscillator

rms Root mean square

A. Appendix

A.1. Datasets for figure 4.5

Table with names of datasets for figure 4.5. Point number corresponds to numbering in figure 4.5, angle difference refers to point 15 (see chapter 6). The raw filenames are retrieved from the timestamp, and are *MGEODAR-<timestamp>.h5*.

Table A.1.: Timestamp of datasets shown in Figure 4.5.

Point Number	angle	timestamp AT on	timestamp AT off
15	0.0	2024-02-06-14-58-01	2024-02-06-14-55-25
14	1.0	2024-02-06-14-53-24	2024-02-06-14-52-39
1	2.0	2024-02-06-13-15-59	2024-02-06-13-16-39
2	4.0	2024-02-06-13-47-45	2024-02-06-13-46-39
3	6.0	2024-02-06-13-52-52	2024-02-06-13-51-47
4	8.0	2024-02-06-13-59-48	2024-02-06-13-58-50
5	7.0	2024-02-06-13-55-57	2024-02-06-13-54-58
6	9.0	2024-02-06-14-03-07	2024-02-06-14-02-08
7	10.0	2024-02-06-14-10-56	2024-02-06-14-10-09
8	11.0	2024-02-06-14-14-42	2024-02-06-14-14-00
9	12.0	2024-02-06-14-18-34	2024-02-06-14-16-37
10	13.0	2024-02-06-14-25-04	2024-02-06-14-20-39
11	14.0	2024-02-06-14-23-06	2024-02-06-14-27-18
12	15.0	2024-02-06-14-31-32	2024-02-06-14-31-00
13	17.0	2024-02-06-14-33-43	2024-02-06-14-33-04
16	-1.0	2024-02-06-15-04-19	2024-02-06-15-02-53
17	-3.0	2024-02-06-15-08-46	2024-02-06-15-07-55
18	-4.0	2024-02-06-15-22-26	2024-02-06-15-20-04
19	-6.0	2024-02-06-15-26-46	2024-02-06-15-26-07
20	-8.0	2024-02-06-15-29-25	2024-02-06-15-28-43
21	-10.0	2024-02-06-15-34-37	2024-02-06-15-33-53
22	-11.0	2024-02-06-15-38-27	2024-02-06-15-37-38
23	-13.0	2024-02-06-15-42-23	2024-02-06-15-40-39

A.2. GPS locations corresponding to datasets for the radar calibration section 4.5

GPS locations corresponding to datasets A.1.

Table A.2.: GPS locations corresponding to datasets from Table A.1. Range indicates the radar range of the peak due to the active target on. Datasets with point number 6 – 13 and 20 – 23 are outside the operational antenna cone, and therefore not range can be determined from radar.

Point Number	Angle [°]	Lat [°]	Lon [°]	Height [m]	Range [m]
15	0.0	47.30794759	11.38105777	1975.52	160.94
14	1.0	47.30793428	11.38110041	1974.85	160.45
1	2.0	47.3079405	11.38114661	1973.44	162.08
2	4.0	47.30792368	11.38119667	1974.87	161.79
3	6.0	47.30792005	11.38126258	1974.94	163.27
4	8.0	47.30790683	11.38136712	1976.37	165.29
5	7.0	47.30791536	11.38132729	1975.88	164.84
6	9.0	47.30790219	11.38139933	1974.31	no peak
7	10.0	47.30791037	11.38144269	1975.05	no peak
8	11.0	47.3079078	11.38148689	1976.57	no peak
9	12.0	47.30791089	11.38153303	1976.84	no peak
10	13.0	47.307907	11.38157917	1976.85	no peak
11	14.0	47.30790619	11.38163526	1977.42	no peak
12	15.0	47.30791489	11.38168204	1977.12	no peak
13	17.0	47.30790217	11.38172992	1977.62	no peak
16	-1.0	47.3079678	11.38102346	1977.02	162.52
17	-3.0	47.30799204	11.38098462	1977.05	164.32
18	-4.0	47.30801917	11.38093125	1978.34	166.42
19	-6.0	47.30804918	11.38086181	1979.04	168.64
20	-8.0	47.30806698	11.38079531	1980.26	no peak
21	-10.0	47.30809422	11.38072384	1981.19	no peak
22	-11.0	47.30810599	11.38067288	1982.12	no peak
23	-13.0	47.30812167	11.38062598	1984.42	no peak

A.3. Tables for Radar settings section 6.3

Measurement points from the 25.06.24 and associated Radar settings.

A.4. Antenna pattern

Active target antenna pattern picture from Novel Wireless Tech.

Table A.3.: Measurement points from the 25.06.24 and associated Radar settings

Baseband	Receiver chain	Transmitter chain	Point number
10|24|0.1|6	16.0|16.0|0.0	27.9|-4.5	1
10|12|0.1|-6	16.0|16.0|0.0	27.9|-4.5	2
21|24|10.2|6	16.0|16.0|0.0	27.9|-4.5	3
21|24|0.1|-6	16.0|16.0|0.0	27.9|-4.5	4
10|24|0.1|-6	16.0|16.0|0.0	27.9|-4.5	5
10|24|0.1|6	16.0|16.0|0.0	27.9|-4.5	6
10|24|0.1|6	16.0|16.0|0.0	22.9|0.0	7
10|24|0.1|6	16.0|16.0|0.0	16.9|0.0	8
10|24|0.1|6	16.0|16.0|0.0	33.4|-9.0	9
10|24|0.1|6	16.0|16.0|0.0	33.4|0.0	10
10|24|0.1|6	16.0|16.0|0.0	33.4|-4.5	11
10|24|0.1|6	-3.0|-3.0|7.0	27.9|-4.5	12
10|24|0.1|6	8.0|8.0|4.0	27.9|-4.5	13
10|24|0.1|6	8.0|16.0|0.0	27.9|-4.5	14
10|24|0.1|6	0.0|16.0|0.0	27.9|-4.5	15
10|24|0.1|6	-3.0|16.0|0.0	27.9|-4.5	16
10|24|0.1|6	16.0|8.0|0.0	27.9|-4.5	17
10|24|0.1|6	16.0|0.0|0.0	27.9|-4.5	18
10|24|0.1|6	16.0|-3.0|0.0	27.9|-4.5	19
10|24|0.1|6	16.0|16.0|4.0	27.9|-4.5	20
10|24|0.1|6	16.0|16.0|7.0	27.9|-4.5	21

Table A.4.: Measurement points from the 25.06.24 and associated Radar settings. For Baseband the format is Stage1|Stage2|Stage3 ...

Point Nr.	Baseband	Receiver	Transmitter	timestamp
1	10|24|0.1|6	16.0|16.0|0.0	27.9|-4.5	13-56-24

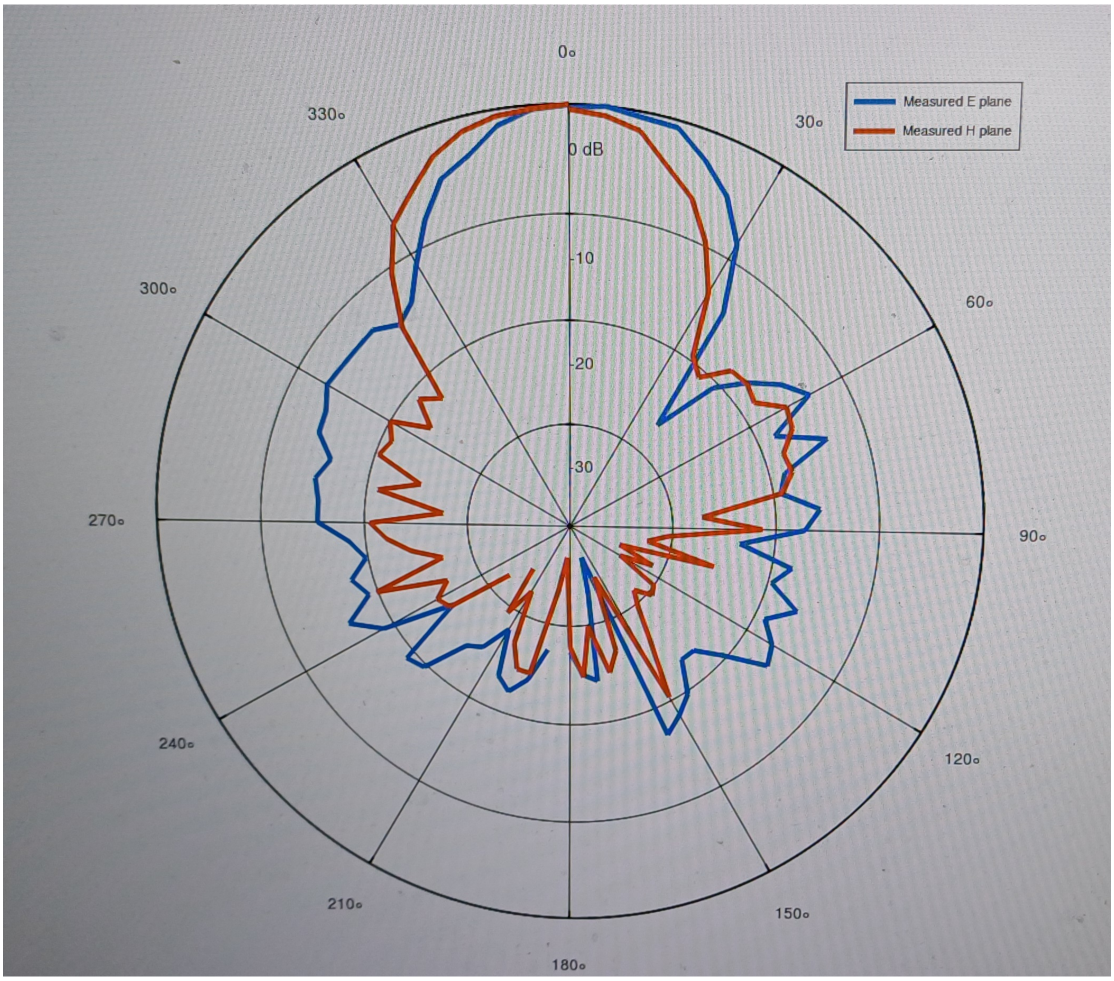

Figure A.1.: Active target antenna pattern with beamwidths around $35°$ and deviation of less than $5\,\%$.